

Syracuse University

SURFACE

Theses - ALL

December 2014

THE EFFECT OF SURFACE ROUGHNESS ON THE FRETTING CORROSION OF 316L STAINLESS STEEL BIOMATERIAL SURFACES

Aarti Shenoy
Syracuse University

Follow this and additional works at: <https://surface.syr.edu/thesis>



Part of the [Engineering Commons](#)

Recommended Citation

Shenoy, Aarti, "THE EFFECT OF SURFACE ROUGHNESS ON THE FRETTING CORROSION OF 316L STAINLESS STEEL BIOMATERIAL SURFACES" (2014). *Theses - ALL*. 79.
<https://surface.syr.edu/thesis/79>

This is brought to you for free and open access by SURFACE. It has been accepted for inclusion in Theses - ALL by an authorized administrator of SURFACE. For more information, please contact surface@syr.edu.

ABSTRACT

The medical device industry is still seeking answers to the mechanically-assisted corrosion (MAC) problem, which becomes increasingly important due to modularity in design. MAC manifests in various forms, some of which are fretting corrosion, crevice corrosion and stress corrosion. Several studies have been conducted to understand the causes and the factors that affect fretting corrosion. Some of the factors are the applied load, surface potential, oxide film characteristics and solution chemistry near the interface. Surface properties such as surface roughness determine the topography of the surface and the nature of asperity-asperity contact, which is a factor that would determine the mechanically assisted corrosion behavior of the interface, like the stem-neck and head-neck taper junctions in modular hip replacement devices. This study aims to understand the correlation between surface roughness of 316L stainless steel samples and fretting corrosion behavior using a variable load pin-on-disc test. It was found that the smoother surfaces are associated with lower fretting currents. However, smoother surfaces also created the conditions for fretting initiated crevice corrosion to occur more readily. Fretting corrosion regimes and the severity are thus dependent upon the surface roughness. A possible explanation could be due to the inverse relationship between the interasperity distance parameter, Δ , and fretting currents. The coefficient of friction between the two surfaces in contact however remained unaffected by surface roughness, but decreased with increasing load. Smoother surfaces, while lowering fretting corrosion reactions can enhance crevice corrosion reactions in 316L stainless steel interfaces.

**THE EFFECT OF SURFACE ROUGHNESS ON THE FRETTING CORROSION OF
316L STAINLESS STEEL BIOMATERIAL SURFACES**

By

Aarti Shenoy

B.E. Biomedical Engineering, University of Mumbai, 2012

Thesis

Submitted in partial fulfillment of the requirements for the degree of
Master of Science (M.S.) in *Bioengineering*

Syracuse University

December 2014

© Copyright 2014 Aarti Shenoy

All rights reserved

ACKNOWLEDGEMENT

I would like to take this opportunity to express my deepest gratitude to everyone who supported me and helped me see this work to completion. First and foremost, I would like to thank my parents, Anjana and Anil Shenoy and my sister, Akshata. It is due to your love, encouragement and patience through the years that have helped me achieve all that I have. I also owe a lot to my friends, who pushed me to excel and helped keep my sanity intact through every difficulty with humor and faith in my abilities.

Without the support of my advisor, Dr. Jeremy Gilbert, I would not have been able to successfully conclude my research. Everything I have learnt as a graduate student so far, I have learnt from my interactions with him. I really enjoyed the talks we would have, discussing ideas and interpreting results. Those talks taught me so much more than just science. He is an inspiration to me and my colleagues who work under his able supervision.

Throughout this arduous journey of performing experiments, analyzing the data and assembling the results into coherent conclusions, I was able to rely upon my colleagues to support, teach and aid me at every step. I want to especially thank Andrew Ferrel, Shiril Sivan and Sachin Mali for their suggestions and for helping me understand the equipment and most of all, for answering all my naïve questions and doubts.

I would like to thank my oral defense committee members: Dr. Michelle Blum, Dr. Julie Hasenwinkel and Dr. Pranav Soman for taking time out of their schedules and for their insights which helped improve this manuscript significantly.

Lastly, I would like to thank the machinists from the Engineering machine shop for helping me by machining the samples and sample sleeves so promptly.

TABLE OF CONTENTS

LIST OF FIGURES	vi
LIST OF FIGURES	viii
1. Introduction & Literature Survey	1
2. Goals & Hypotheses	8
3. Surface Roughness studies	
3.1 Introduction & Motivation	9
3.2 Materials & Methods	11
3.3 Results	18
3.4 Discussion	36
3.5 Conclusion	40
4. Summary	41
5. Appendix	43
6. Bibliography	49
7. Vitae	55

LIST OF FIGURES

Figure 1:	Schematic of Pin-On-Disc (POD) test system comprised of mechanical and electrochemical components	11
Figure 2:	Plot of current density vs. time as displayed in CorrWare	18
Figure 3:	Typical current vs. time graph for a single fretting period for a 316L stainless steel pin and disc couple	19
Figure 4:	Average fretting current vs. average load for 316L stainless steel pin and disc couples for $V = 0$ mV vs. Ag/AgCl	20
Figure 5:	Typical current vs. time graph demonstrating a continuation of corrosion reactions after a single fretting period for a 316L stainless steel pin and disc couple	21
Figure 6:	Fretting current density graphs for each grit level for the first 4 loads (0.5 N, 1 N, 2 N and 4 N) to demonstrate fretting initiated crevice corrosion	22
Figure 7:	Fretting loops corresponding to 5 different loads for pin and disc couples at (a) 240 grit (b) 320 grit and (c) 600 grit	23
Figure 8:	Average work done vs. nominal contact stress for 316L stainless steel pin and disc couples	24
Figure 9:	Average current density vs. average work done for 316LSS samples with roughness 240 grit, 320 grit and 600 grit	25
Figure 10:	Average coefficient of friction vs. average load applied for 316L stainless steel couples at 240 grit, 320 grit and 600 grit	26
Figure 11:	Average interasperity distance vs. average load for 316L stainless steel couples at 240, 320 and 600 grit	27

Figure 12:	Average fretting current vs. average interasperity distance for 316L stainless steel couples at 240, 320 and 600 grit	28
Figure 13:	Average fretted area for samples of 240 grit, 320 grit and 600 grit	29
Figure 14:	AFM images denoting height and deflection measurements of 316L stainless steel 240 grit surface	30
Figure 15:	AFM images denoting height and deflection measurements of 316L stainless steel 320 grit surface	31
Figure 16:	AFM images denoting height and deflection measurements of 316L stainless steel 600 grit surface	31
Figure 17:	Secondary electron SEM micrographs of (a) pin and (b) disc with 600 grit surface roughness post test (c) low magnification image of pin showing actual area of contact	32
Figure 18:	Secondary electron SEM micrographs of (a) 240 grit disc (b) 600 grit disc (c) magnified region of disc in (a) and (d) magnified image of disc in (b)	33
Figure 19:	Backscattered electron SEM micrographs of (a) 240 grit disc (b) 320 grit disc (c) 600 grit disc post-test	34

LIST OF TABLES

Table 1: Calculation of weight fraction of major elements in 316L stainless steel.....	15
Table 2: Properties of major alloying elements present in 316L stainless steel	15
Table 3: Calculation of alloy oxide properties from alloying element oxide values ...	16
Table 4: Surface roughness parameters measured using Eqns. 2.2 and 2.3 for 316LSS coupons using AFM in contact mode	30

1. INTRODUCTION AND LITERATURE SURVEY

Orthopedic devices such as bone plates, screws, intramedullary nails as well as joint replacement systems are mainly designed using alloys such as stainless steel (316LSS), cobalt-chromium alloys (CoCrMo) and titanium alloys (Ti6Al4V, TiAlNb). The primary reason behind this is their mechanical properties pertaining to load-bearing and modulus as well as their corrosion resistance. Current designs of metallic medical devices often have multiple metal-on-metal contacts (eg: head-neck taper, neck-stem taper, screw-countersink). Along with modifications in design, various metal-metal combinations are also used in different components depending on the application and other design factors.

However there are instances of failure in these systems, often before the expected lifetime of the device. Failure of the device leads to loss of load bearing ability, instability or loosening of the implant and deterioration of the joint. This is manifested in the form of physiological indications such as pain in the joint, inflammation, loss of bone tissue or osteolysis and pseudotumors, to name a few. Such failure of the device necessitates a revision surgery, where the failed device is replaced by a new device. Studying retrieved implants has revealed corrosion and wear of many device surfaces to be one of the main causes [1]–[7]. Such corrosion can be the result of mechanical and electrochemical interactions between the different components of these systems and hence the problem of mechanically assisted corrosion (MAC) needs to be better understood.

MAC can occur in various forms depending on the primary cause which includes but is not limited to tribocorrosion of bearing surfaces, rubbing of device against bone tissue, etc. However the consequence of MAC may be detrimental to the performance and structure of

the device, and often leads to mechanical failure, corrosion by-products in the biological environment and wear debris among others. One of the forms of MAC is fretting corrosion, where micromotion ($<100\text{ }\mu\text{m}$) between interfacing surfaces can lead to development of electrochemical conditions leading to breakdown of the oxide films on the surfaces of the alloys. Such breakdown promotes the oxidation of the metallic surface and can lead to increased corrosion before repassivation can restore the oxide film.

Some factors affecting fretting corrosion include interfacial load, surface potentials, oxide film characteristics, solution chemistry in the vicinity and surface characteristics as well as the constituent materials. Surfaces in contact have asperities, which determine the actual area of contact affecting corrosion at the interface as opposed to the nominal area of contact. Crevices formed at taper junctions, for example, result due to tight fits and short interfacial distances between surfaces and can lead to accumulation of ionic species, changing pH and may affect the potential at the surfaces.

Corrosion resistance of metallic biomaterials is attributed to the presence of a passivating nanometer-scale oxide film on the surfaces of these alloys that limits susceptibility to corrosive attack in the human body. However, stainless steel was acknowledged as having lower corrosion resistance than cobalt-chromium and titanium alloys and as being more prone to pitting attacks [8]. Even so, stainless steel is still widely used in fracture fixation devices and surgical instruments due to its relative advantages such as ease of availability, strength, elastic modulus and low cost.

There are several reasons for studying the corrosion behavior of stainless steel. Savarino et al., in 2008 concluded that a high level of chromium and nickel ions was found in the serum of patients with malfunctioning stainless steel plates [9]. Jones et al., in 2001

evaluated the relevance and clinical significance of periosteal reaction and osteolysis in patients with an implanted intramedullary nail. They concluded that the presence of corrosion products and high chromium ion levels in the serum is a major factor in the osteolysis and is an indicator of corrosive wear of the device [10]. The presence of corrosion by-products is sometimes accompanied by the mechanical failure of the implanted devices, increasing the need for revision surgeries. There are several other retrieval analyses that support these findings and make mechanically assisted corrosion a major reason for device failure in vivo [11]–[15].

Mechanically assisted corrosion (MAC) is typically initiated by a mechanical event such as loading or oxide abrasion or a combination of the two. A major form of MAC is fretting corrosion, where mechanical fretting or micromotion ($<100\text{ }\mu\text{m}$ displacement) leads to the abrasion of the passivating oxide film on the alloys surface, thus exposing the underlying metal to corrosive conditions. Usually, if the surface is in a passivating environment (pH and surface potential is within passivating range) the oxide film is reformed within milliseconds. However, with increasing modularity in designs, crevice-like geometries are created at the head-neck and stem-stem conical taper junctions. In these highly restrictive regions, the effects of loading, solution chemistry and motion take on more importance. Fretting corrosion attack is highly localized and is dependent upon the contact area and interfacial motion within that area [16].

For all orthopedic alloys such as CoCrMo or Ti6Al4V or 316LSS, mechanical fretting leads to oxide fracture. Walczak et al hypothesized that repassivation takes place almost instantaneously, however for stainless steel, the oxide formed after fretting is usually FeO instead of Cr_2O_3 . They concluded that FeO being less stable and less robust than Cr_2O_3 ,

does not protect the surface as well. Thus, repassivation of 316LSS surfaces does little to mitigate the damage caused by mechanical fretting [15]. The reformation of the oxide film is also accompanied by a charge transfer, along with release of cations from the surface. These reactions attract the Cl^- ions promoting a high concentration of Cl ions in the crevice of taper junctions, as hypothesized in previous retrieval studies [12], [17]. A pH gradient is then formed (acidic to basic), along with a potential gradient (anodic to cathodic) which creates aggressive conditions within the crevice. When the potential at the surface enters the transpassive region, the passivating oxide layer may or may not be present. With increasing surface potentials, the surface becomes vulnerable to oxide film dissolution due to pitting attack.

The restricted geometries prevent the flushing and replenishment of solution from outside, thus creating a highly acidic environment which further promotes corrosion. This correlation between fretting corrosion and crevice corrosion has been corroborated in previous literature [14], [16], [18], [19]. Pitting attack has been observed in all orthopedic alloys in vivo [20], [21], but more so in stainless steel [15], [16]. It is a form of highly localized corrosion, leading to the dissolution of the oxide film and formation of very small holes in the surface of the alloy. Depassivation of a small area leads to development of anodic potential in the small area and a comparatively large cathodic region which leads to aggressive corrosion just under the depassivated region, forming a pit. If the pit grows fairly large in size, surrounding solution can get entrapped within emulating crevice conditions.

Some factors that are thought to affect fretting corrosion and crevice corrosion are material combinations [12], [17], [22], surface potential [23], [24], applied normal load at the interface [22] and surface properties like topography, coatings and chemistry. In order to

improve the corrosion resistance of orthopedic devices, surface coatings and treatments have been explored. Hashemi et al in 2011 concluded that nitriding the 316L stainless steel at 570°C with prior shot peening enhances the hardness and corrosion resistance of the substrates. Shot peening is a form of surface treatment that introduces residual stresses surface layers and assists the formation of hard phases [25].

In 2014, Chang et al explored the benefits of CuAlO₂ coatings for improving mechanical and electrochemical properties of 316L stainless steel. They found that these coatings enhanced the hardness by 46% with a 200 nm thick CuAlO₂ film. Along with this, the film also raised the E_{corr} that is the potential at which corrosion is initiated, to -0.24V vs. a saturated calomel electrode (SCE) as reference in Ringer's solution from -0.49V vs. SCE for bare 316L stainless steel substrates. The i_{corr} was also improved by two orders of magnitude. Thus a marked improvement can be attained by coating CuAlO₂ on stainless steel, enhancing their corrosion resistance and mechanical properties [26]. Similar coatings and surface treatments are being explored and developed specifically for 316L stainless steel to enhance surface properties and mitigate corrosion [27]–[31].

There is, however, a lack of understanding of how surface roughness and topography influences the corrosion behavior of stainless steel or vice versa. Although surface roughness is understood to be a factor in determining how a surface would behave under corroding conditions, the exact correlation between the roughness and corrosion behavior is not understood well. Conradi et al created a composite coating using silica nanoparticles in an epoxy resin matrix which was proven to improve the hardness and corrosion resistance of the surface. They proposed that the increased surface roughness coupled with enhanced hydrophobicity of the epoxy coating lead to the improvement in corrosion resistance [31].

Swaminathan and Gilbert [22] studied the interaction of electrochemical and mechanical factors that describe fretting corrosion using the following equation:

$$I_{film} = 2 \frac{\rho n F}{M_w} \frac{V_{nom}}{\Delta} \frac{d\delta}{dt} = 4 \frac{\rho n F}{M_w} \frac{V_{nom}}{\Delta} d\nu \quad (\text{Eqn. 1.1})$$

The interasperity distance, denoted by Δ , is the average distance between individual asperities within the area of contact in the sliding direction. The fretting current I_{film} is calculated based on the oxide properties such as the oxide density (ρ), valence state of cation (n) and molecular weight (M_w), the sliding distance (d), frequency of fretting (ν) and the nominal volume of oxide abraded (V_{nom}). Thus fretting corrosion is understood to be a function of the material combination, the abrasion rate which varies with the applied load as well as the magnitude and frequency of micromotion, the repassivation rate of the oxide at the prevalent surface potential and the surface topography of the surfaces in contact.

In order to gain a better understanding of the factors affecting fretting corrosion in orthopedic alloys, in particular 316L stainless steel, the present study focuses on the effects of the roughness of the surfaces in contact as well as different material combinations. The fretting regimes and mechanisms as well as electrochemical and mechanical parameters associated with fretting corrosion were studied using a pin-on-disk test system, developed in-house. The goals of the study were to determine if changes in surface roughness had an effect on the corrosion of the 316L stainless steel surfaces in contact. The mechanical and electrochemical parameters associated with corrosion of the surfaces in contact were determined by a pin-on-disk test system developed previously.

In this study, the surface roughness of the 316L stainless steel couples are modified to achieve different Ra values. Modifying the surface roughness would modify the surface

topography since the roughness is essentially a quantitative description of the topography.

The surface topography is interconnected with surface energy and in turn, is a determinant of the interactions a surface will have with its surroundings. Interaction with the encompassing solution as well as the ions, proteins, cells in the solution is dependent on the surface energy and indirectly, on the surface topography and roughness. There are examples in the literature that demonstrate these ideas [32]–[35]. It is essential, therefore, to understand the correlation between surface roughness and fretting corrosion behavior. The fretting regimes as outlined by Vingsbo and Soderberg in 1988 observed during individual fretting experiments are also described [36].

How micromotion affects surface topography and modifies the roughness would, in turn, determine the interaction of the surface with the surrounding. It is also important to note how the fretting corrosion behavior changes with different surface roughness. The interactions between a rough surface and a smooth surface or that between two rough surfaces, for example, would be different from each other. Two rough surfaces would demonstrate higher friction and possibly more wear than the interaction between a rough and smooth surface. The compliance of the surfaces would also affect these interactions, that is, hard surfaces might slide more easily than elastic surfaces or vice versa. In this way, interactions of different topographies will vary which can affect the electrochemical and mechanical characteristics.

2. GOALS AND HYPOTHESES

The specific goal of this study and the underlying hypotheses are as follows:

1. To determine the effects of surface roughness of 316L stainless steel couples on the overall fretting corrosion behavior, including fretting regimes and mechanisms.

Hypotheses:

- Surface roughness affects the crevice geometry which affects fretting corrosion reactions and the mechanisms of fretting
- Tighter crevices from smoother topography may entrap surrounding solution and create more aggressive conditions that promote corrosion and might lead to pitting of the surface.
- Asperities in contact and the distances between individual asperities affect the distribution of loads and development of contact stresses. Asperities placed closer to each other give rise to higher fretting currents and accelerate fretting corrosion.

3. SURFACE ROUGHNESS STUDIES

3.1 Introduction:

The presence of an oxide film on the surface of passivating metals kinetically slows the corrosion of the substrate. Hence, it is reasonable to assume that the properties of the surface have a significant effect on the corrosion of the underlying metal. One might say that the surface determines how the entire device would perform in vivo, under varying conditions. The physical, morphological and chemical properties of the surface determine how the metal reacts to corroding conditions, or to physical stimuli like abrasion and loading which are the triggers for fretting corrosion.

Some of these factors are oxide thickness, oxide composition, surface potential and surface roughness. In this study, the surface roughness is explored as a factor in fretting corrosion and how surfaces with different surface roughness values will corrode. Surface roughness affects the interaction of the surface with interfacing surfaces, alters the local crevice geometry and the adherence of proteins, cells and ions that may be present at the interface. The roughness of surfaces in contact may also affect the interfacial friction, thus impacting the relative motion of surfaces in contact as well as wear and corrosion resulting from the motion.

Fretting between interfaces is influenced by the actual area in contact, depending on the individual asperities on a surface corresponding to the asperities on the interfacing surface. Rougher surfaces may or may not have more asperities but the volume confined by consecutive asperities will be larger when compared with a smooth surface. The solution chemistry resulting from smaller crevices may promote crevice corrosion. In terms of

nominal contact area vs. the actual area in contact, the area in contact will depend on the area at the peak of each asperity and the overall summation of all asperities on a surface. The smoothness of a surface may be a factor of how sharp the asperities are and this will change the surface area available.

The results of pin-on-disk tests on 316L stainless steel couples with different surface roughness values are presented here, followed by a discussion on their implications. An analysis is carried out to determine the dependence of the fretting currents, coefficient of friction and fretting regimes on surface roughness. Scanning Electron Microscopy (SEM) images are obtained in secondary and backscattered electron modes prior to and post-test to visualize the fretting area and fretting scars caused on the surface, and to find a correlation between surface roughness and fretting damage. Surface roughness was measured prior to testing using contact mode Atomic Force Microscopy (AFM).

3.2 Materials and Methods:

The samples tested were 316L stainless steel (ASTM F138) discs (35 mm diameter) and cone shaped flat bottomed pins (interfacing surface diameter nominally: 0.5 mm to 1 mm). Each test surface (disc and pin) was sanded by hand to different grits, using emory paper of 240, 320 and 600 grit. After polishing, the samples were cleaned with ethanol and DI water to get rid of any particulates from the sanding where the scratches were aligned in a single direction. Only the test area along with some surrounding area was exposed, approximately 0.079 cm^2 , while the rest of the surface was covered using an acrylic coating. This was done in order to have uniform test areas for every trial at all the grit levels. Three trials were performed at each grit level. Pre-test imaging was done using SEM to determine the area exposed for fretting as well as to visualize the surface topography prior to fretting. The following diagram is a schematic of the test system used:

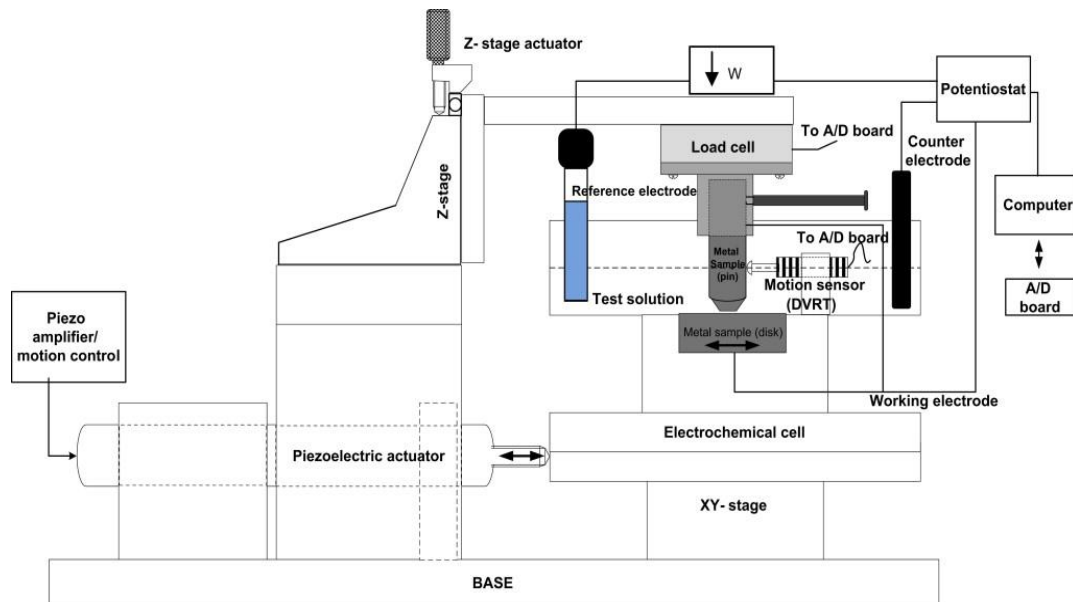


Fig 1: Schematic of Pin-On-Disc (POD) test system comprised of mechanical and electrochemical components [adapted from Swaminathan & Gilbert, 2012]

The above system combines components for both electrochemical and mechanical characterization. The electrochemical cell is mounted rigidly as shown on a linear X-Y stage (Newport Inc., USA) to which the sliding motion of 50 μm at 1.25 Hz is applied as a sine wave generated by a waveform generator, amplified using a piezoelectric amplifier and supplied to a piezoelectric actuator (Piezo-Jenna System, Germany). The actuator is able to apply consistent and accurate motion of up to 140 μm to the stage, which is required to simulate fretting micromotion. This motion is measured using a direct variable reluctance transducer (DVRT, Microstrain Inc., USA). This is a highly sensitive device with a resolution of $\pm 4 \mu\text{m}$ to measure the relative motion of the cylindrical portion of the pin with respect to the base of the cell.

The normal load between the pin and disc is measured using a six-axis load cell (MINI 45 F/T six axis load cell, ATI Measurement Inc., USA) which is mounted rigidly on the Z-stage and holds the sample pin. It measures the tangential and normal loads produced as a result of loading and motion. The pin-and-disc configuration is loaded manually using a micrometer screw by the movement of the pin along the Z-axis by the Z-stage actuator. The forces developed as a result of fretting such as normal force, interfacial tangential force and other moments developed at the pin-and-disc interface must be tracked accurately to determine the interfacial conditions. These conditions vary depending upon the solution conditions and changes in the interfacing surfaces. These measurements are useful in calculating the nominal contact stress, work done during fretting cycles and to ascertain the fretting regimes prevalent during different stages in the fretting test.

The electrochemical cell uses a three-electrode system with the sample disc and pin comprising of the working electrode, a carbon counter electrode and an Ag/AgCl reference

electrode. 60 mL of Phosphate buffered saline (PBS) at pH=7.4 and room temperature is used as the solution. In order to ensure electrical isolation of the sample, the cell is made of delrin and is designed to secure the isolation of the sample disc and pin from the mechanical system. The pin and disc are electrically connected with a wire to ensure connectivity even when they are not in physical contact. The tests are performed under potentiostatic conditions at 0 mV vs. Ag/AgCl reference. The potentiostat (Solartron 1280C Potentiostat/Frequency Response Analyzer, Solartron Analytical Inc., USA) is used to apply the potentiostatic conditions and to measure the currents arising during the fretting period. Data acquisition and analysis is conducted using an independent data acquisition card and a software (CorrWare 2.0/CorrView 2.0, Scribner Associates).

The experimental design involved varying the applied normal load between the pin and disc from 0.5 N to 30 N. The pin and disc were set up such that the grit lines on the surface of the pin were aligned perpendicular to those on the surface of the disc. Prior to testing a rest period of 15 min was allowed with no physical contact between the pin and disc to allow the surface potential to settle around 0 mV vs. Ag/AgCl. Sliding motion along X-axis of 50 μm amplitude at a fretting frequency 1.25 Hz was applied at each load for a period of 60 sec followed by a recovery period to allow the currents to return to baseline, which is the current value prior to fretting.

The raw data was collected and collated using CorrWare for the electrochemical parameters and a custom written NI LabVIEW virtual instrument for the mechanical parameters. The NI LabVIEW program window displays plots of: normal load applied between pin and disc by load cell, tangential forces resulting from the normal load applied, a plot representing the interfacial co-efficient of friction (COF), piezoelectric actuator input to

the stage in terms of voltage and the displacement measured by the DVRT. From the data collected using this program the following parameters and graphs are calculated: COF vs. normal load, work energy vs. nominal contact stress. Work energy is calculated from fretting loops as the hysteresis energy under tangential force-displacement plots. Nominal contact stress is calculated using applied normal force as measured and fretted area measured at the end of each test. The experimental parameters such as the voltage and area exposed is entered into the system by the potentiostat using the CorrWare program. The CorrWare program displays plots of current, voltage, impedance, etc. as they are measured by the potentiostat. Data is analyzed to generate the following plots: average fretting current vs. load applied, average current density vs. nominal contact stress, average current density vs. work done.

An important aspect of this study involved the correlation of interasperity distance, denoted by Δ , and the fretting currents generated during the test. In order to calculate Δ , characteristics of the oxide film such as the molecular weight, density, valence state (or charge per cation) need to be calculated. To do so, the major alloying elements and their weight fractions are determined, the elements that contribute less than 3% by weight are not considered. Elements such as Fe (63%), Cr (18%), Ni (14%) and Mo (3%) are considered as the major contributors to the oxide film on 316L stainless steel. The most prevalent form of oxide is then used to calculate the required oxide parameters.

Element	Atomic Wt. (g/mol)	Weight Fraction (%)	Wt. Fraction of Alloying Element	Mole	Mole Fractions
Fe	55.845	63	0.63	0.0113	0.5717
Cr	51.999	18	0.18	0.00346	0.1754
Ni	58.6924	14	0.14	0.00238	0.1209
Mo	96	3	0.25	0.00260	0.1320
		100.8145	Total moles:	0.019732314	

Table 1: Calculation of weight fraction of major elements in 316L stainless steel. Other alloying elements such as P, Mn, Si, C are not considered in this calculation since their weight fraction is lower than 3%.

From these elements, the most prevalent form their oxides are used to calculate individual characteristics as follows:

Element	Major form of oxide	Mol weight (g/mol)	Density (g/cm ³)	Valence, n
Fe	FeO	71.844	5.24	2
Cr	Cr ₂ O ₃	152	5.22	3
Ni	NiO	74.63	6.67	2
Mo	MoO ₃	143.94	4.69	6

Table 2: Properties of major alloying elements present in 316L stainless steel. The most commonly found oxide forms of these elements are considered for the calculation.

To determine the values for the 316L stainless steel passivating oxide, above values are used.

Oxide present	Density (g/cm ³)	Mw (g/mol)	Valence, n
FeO	5.24	71.844	2
Cr ₂ O ₃	5.22	151.99	3
NiO	6.67	74.628	2
MoO ₃	4.69	143.94	6
Alloy oxide	4.878901	82.4236	2.70332713

Table 3: Calculation of alloy oxide characteristics from alloying element oxide values.

Molecular weight, density and valence are determined by adding the product of individual oxide values and the weight fraction of the element. In the case of Cr₂O₃, the product of the weight fraction of Cr and the molecular weight, density and valence is divided by 2 since two atoms of Cr/molecule of oxide are present.

These averaged values then determine the charge per volume of oxide present as follows:

$$\text{Charge per volume of oxide} = \frac{\rho * n * F}{M_w} \quad (\text{Eqn. 2.1})$$

Where, M_w= Molecular weight of oxide

ρ= density of oxide

n= valence of oxide

F= Faraday's constant= 96500 Coulombs

The charge per volume of oxide is an important parameter in the calculation of Δ. The amount of oxide abraded and formed due to repassivation is a determinant of the currents generated during fretting corrosion.

The surface roughness parameters, R_a and R_q (nm) were measured for 316L stainless steel surfaces polished with 240, 320 and 600 grit paper. Contact mode Atomic Force Microscopy (AFM) was used to do so, and the samples to be used for measurement were

specially prepared to be thinner than 4 mm and have a diameter lower than 10 mm. Three images were obtained per sample, with an area of 25 x 25 μm ; all three images were obtained from the central portion of the coupon. The two parameters measured represent the surface roughness in different ways: R_a is the arithmetic average of absolute height values and R_q is the root-mean-squared value of absolute height values. Thus, three values for each were acquired and one-way ANOVA was carried out to test the difference in the roughness.

$$R_a(nm) = \frac{1}{n} \sum_{i=1}^n |Z_i - Z_{avg}| \quad (\text{Eqn. 2.2})$$

$$R_q(nm) = \sqrt{\frac{1}{n} \sum_{i=1}^n |Z_i - Z_{avg}|^2} \quad (\text{Eqn. 2.3})$$

where, n = number of data points acquired within desired area

Z_i = individual height values of asperities on surface of interest

Z_{avg} = average height value for all asperities on surface of interest

Finally, images of the pre-test and post-test surfaces were obtained using Scanning Electron Microscopy (SEM) in secondary electron and backscattered electron mode to characterize the fretting scars and fretted area. ImageJ, an imaging software, was used to measure the actual fretted area which was necessary to determine the work done and contact stress at each load applied. It is important to note that only the final fretted area, measured at the end of each test, is used to make area estimates, for example, in calculating nominal contact stress or the work done or energy dissipated during fretting. Surface morphology and its changes due to fretting corrosion and wear were observed, as was pitting and plastic deformation and their extent. Statistical analysis was conducted using two-way ANOVA, with the surface roughness and the applied load as factors, to determine the dependence of

fretting currents and coefficient of friction on the roughness of the surfaces in contact.

Results with $p < 0.05$ was considered as significant.

3.3 Results:

In this section, the results of the POD tests on 316L Stainless steel couples at different surface roughness levels are described.

3.3.1 Fretting current data and analysis:

Fig. 2 shows the typical currents measured during a fretting corrosion test, in this case, for the first set of loads in a trial of a 240 grit test sample. Note the different current levels in the plot. The initial portion of the graph is the baseline current prior to the fretting. Another important observation is the different recovery periods after each fretting cycle.

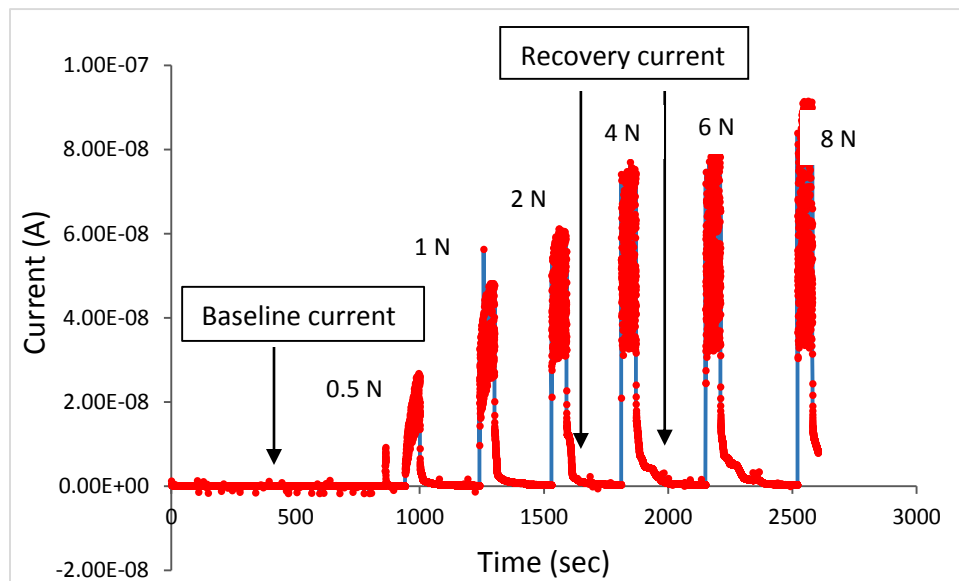


Fig 2: (Raw data) Plot of current density vs. time as displayed in CorrWare. Initial flat portion of the graph is the baseline current density, before fretting. Each current excursion the elevated current produced during fretting at increasing normal loads, beginning with 0.5N and going up to 8N.

Fig. 3 shows the fretting current excursions seen for a single load during a fretting test. This current rise is typical for all orthopedic alloys at most loads, although the

magnitude of the currents varies depending on the mechanical and electrochemical conditions prevalent.

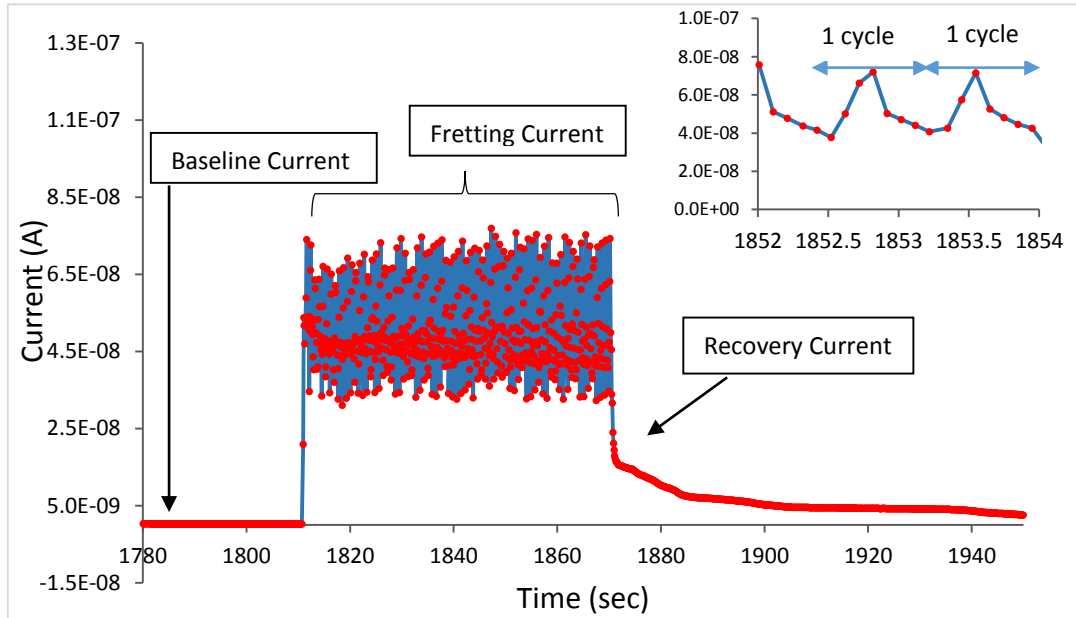


Fig 3: (Raw data) Typical current vs. time graph for a single fretting period for a 316L Stainless steel pin and disc couple. Fretting time is approximately 60 sec followed by a rest period to allow the current to attain baseline value. Also the inset shows two individual cycles of fretting for the entire fretting period shown here.

In Fig. 3, the fretting corrosion at load 4 N for a sample at 240 grit is shown. The graph is comprised of three separate parts. The first part is the baseline current prior to fretting, which in this case starts around 1810 sec. The second portion is the elevated current, which is approximately 45 to 65 nA in this graph. The individual current values recorded at each point are averaged over the entire fretted period for a particular load to obtain an average current value. The third part of the graph is the recovery to baseline current post fretting. The difference of the combined average of the two baseline values (before and after fretting) and the average elevated current value is the average fretting current at that particular load.

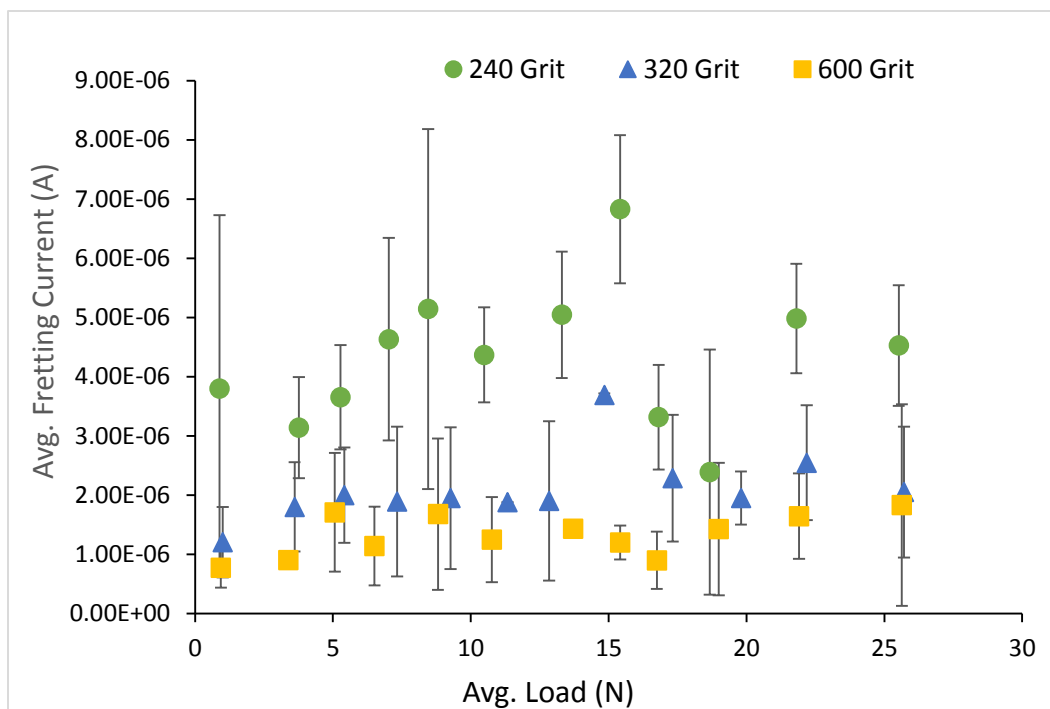


Fig 4: Average fretting current vs. average load for 316L stainless steel pin and disc couples for $V = 0$ mV vs. Ag/AgCl. Plots for 240, 320 and 600 grit trials are displayed. The currents measured over fretting period are divided into windows based on loads 2 N apart from 0.5 N to 30 N. Data were averaged over each window to obtain the average current at each average load. Average currents: (a) 4 μ A at 240 grit (b) 3 μ A at 320 grit (c) 1 μ A at 600 grit.

Fretting currents are dependent upon surface roughness with smoother surfaces producing lower fretting currents. This can be seen in Fig. 4 where the average fretting current at each grit level is plotted against the average normal load applied. The current values remain more or less constant over the range of loads at a particular surface roughness. As seen here the smoother surface, that is the surface polished with 600 grit paper, demonstrated statistically significant lower fretting currents than the rougher surfaces (240 and 320 grit) ($p < 0.005$). The currents generated also vary with applied load and showed a significant dependence on the load ($p < 0.05$). Currents increase with increasing load up to a peak value, after which the currents drop with increasing load.

In some cases (see Fig 5), prolonged crevice initiated corrosion is observed. This form of corrosion continues after ending of the fretting action, which indicates continuing crevice corrosion as described previously in chapter 1. The minimum normal load at which prolonged crevice corrosion after the end of fretting motion is observed is the onset load for the continued corrosion.

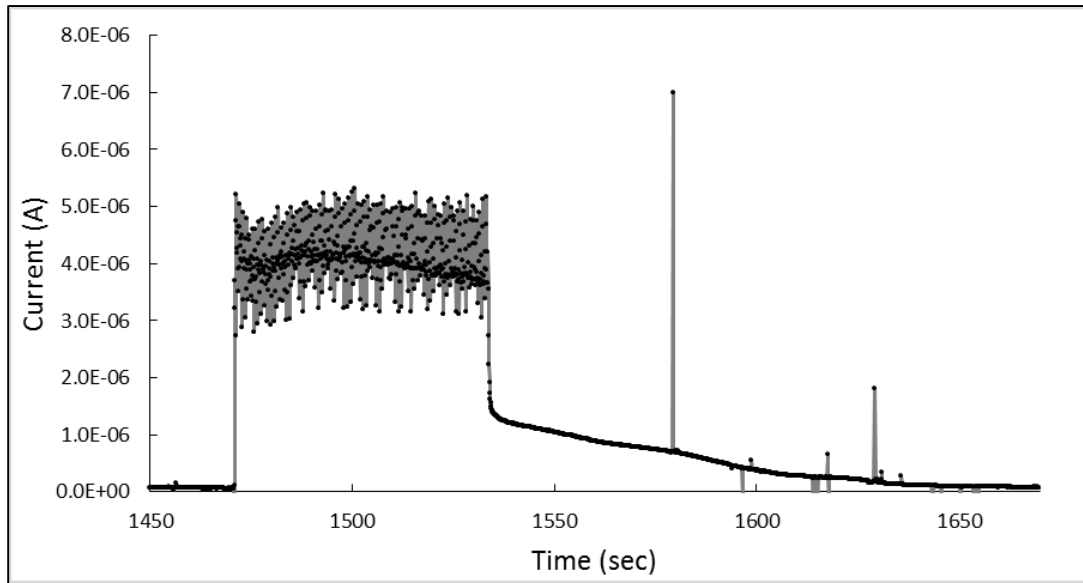


Fig 5: (Raw data) Typical current vs. time graph demonstrating a continuation of corrosion reactions after a single fretting period for a 316L stainless steel pin and disc couple. Fretting time is approximately 60 sec followed by a recovery period to allow the current to return to the baseline value. Return to baseline is delayed in this case due to continued corrosion at the interface in spite of no fretting motion.

From Fig. 6(a), 6(b) and 6(c), it was observed that the onset load for fretting initiated crevice corrosion varied with the surface roughness of the samples. The onset load for rougher surfaces (240 and 320 grit) was higher (4 N in both cases) whereas for the smoother surface (600 grit) the onset load was lower (1 N). The return to baseline also took longer in the case of the smoother surface, around 80 sec in 600 grit samples compared to around 35

sec in 240 and 320 grit samples. Similar results were seen for all the trials at all grit levels.

Thus, fretting leads to more aggressive crevice corrosion in smoother surfaces and this occurs at lower loads for smoother surfaces.

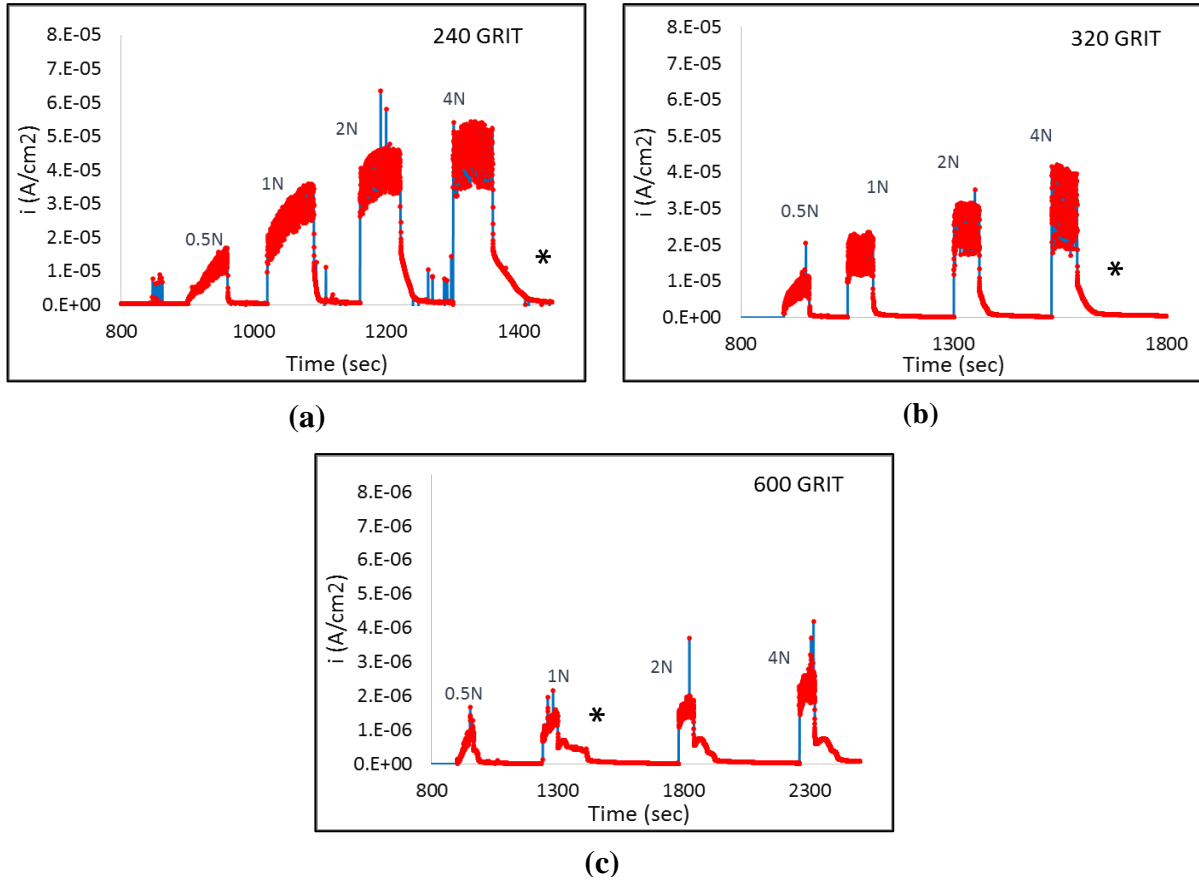


Fig 6: Fretting current density graphs for each grit level for the first 4 loads (0.5 N, 1 N, 2 N and 4 N) to demonstrate fretting initiated crevice corrosion (*). Current magnitude is lower for 600 grit and the crevice corrosion more prolonged. Onset loads: (a) 4 N for 240 grit (b) 4 N for 320 grit (c) 1 N for 600 grit

3.3.2 Work done and fretting regimes

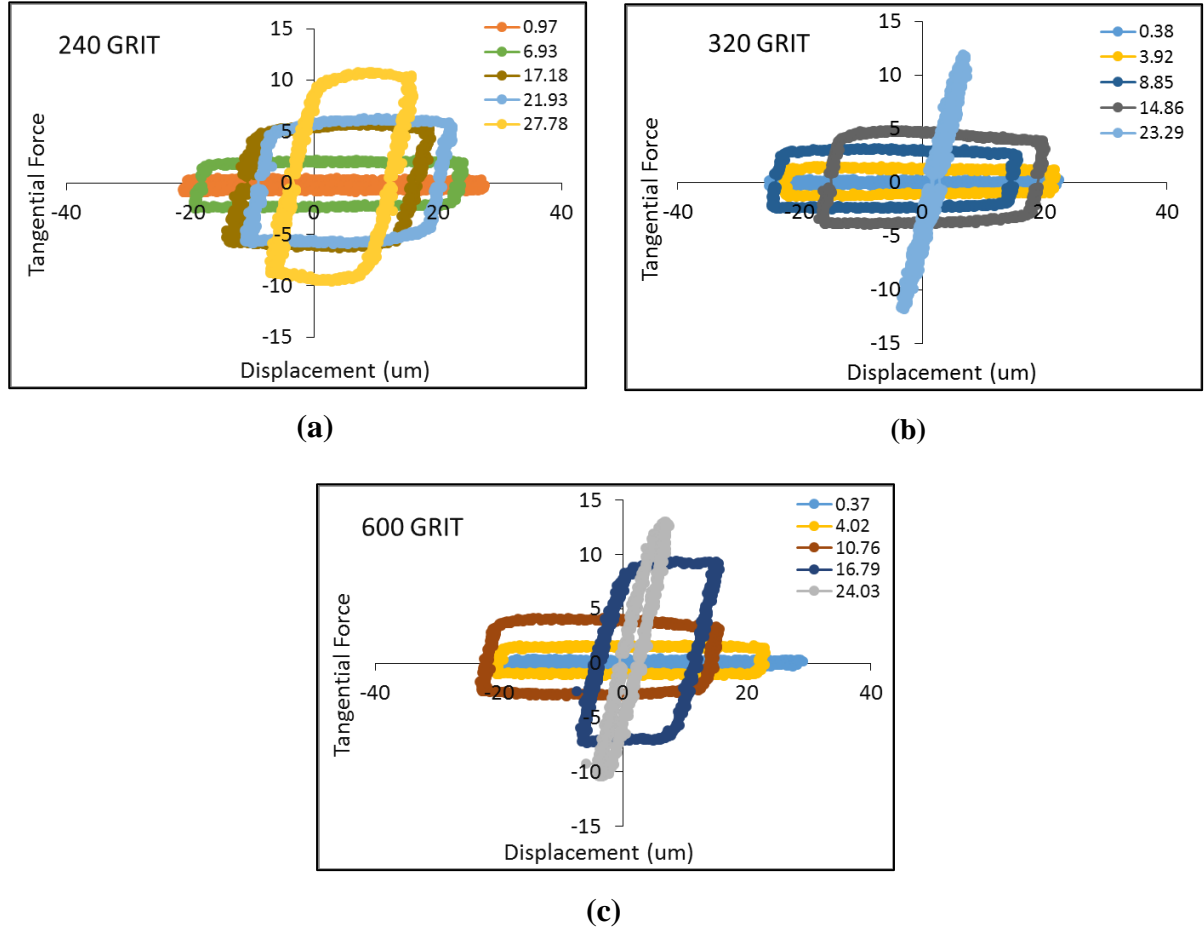


Fig 7: Fretting loops corresponding to 5 different loads for pin and disc couples at (a) 240 grit (b) 320 grit and (c) 600 grit. The tangential force data measured at a certain load over the entire fretting period for that load is plotted against the pin displacement measured from the starting point of the pin at the beginning of fretting.

Figure 7(a), 7(b) and 7(c) are representative plots of fretting loops obtained by plotting tangential force at individual loads against the displacement of the pin relative to the disc at that load during fretting to obtain hysteresis loops. The area enclosed within any individual loop is the amount of energy dissipated or the work done for conversion of mechanical energy into electrochemical and other forms of dissipative energy (like heat).

From these loops it is seen that at low normal loads the pin is able to cover a full range of motion (50 μm displacement), performing a full slip regime. The amount of work done is low due to the low applied load. As the load increases, the range of motion is restricted due to sticking of the pin, demonstrating the stick-and-slip or partial slip regime. For smoother surfaces (320 and 600 grit) at high loads, the pin is seen to be stuck and is unable to displace, instead the surfaces undergo elastic deformation and hence minimal work is done.

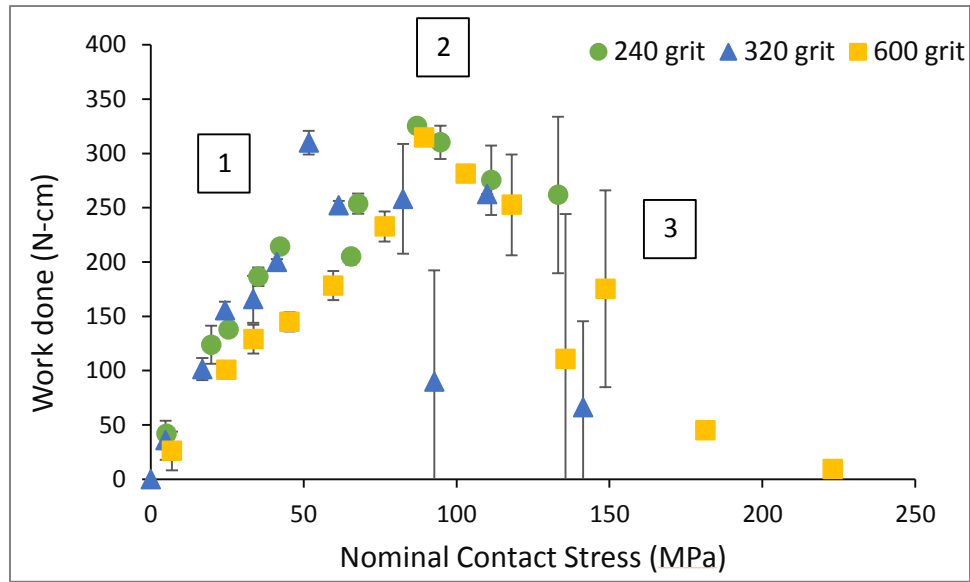


Fig 8: Average work done vs. nominal contact stress for 316L stainless steel pin and disc couples. Plots for 240, 320 and 600 grit trials are displayed. The three fretting regimes seen in the above plot are [1] full slip [2] partial slip and [3] complete stick. Mean and SD n=3.

Fig. 8 summarizes the fretting regimes observed as well as the amount of work done in each regime. It is seen that during full slip (region 1, Fig. 8), the work done increases with increasing nominal contact stress (load divided by fretted area measured at the end of the test) which is also evidenced by the area enclosed within corresponding fretting loops. The work done reaches a maximum value during the partial slip regime (region 2, Fig. 8) and then starts to decline as seen in the complete stick regime (region 3, Fig. 8). The fretting loops at

higher loads for 600 grit are therefore thinner showing minimal or no slip displacement.

There is no significant dependence of the work done on the grit level of the sample surfaces at lower loads, however for higher loads, the work done is much lower for smooth surfaces.

3.3.3 Correlation of mechanical and electrochemical components

During fretting the energy dissipated can be attributed to the mechanical work done and the electrochemical currents generated.

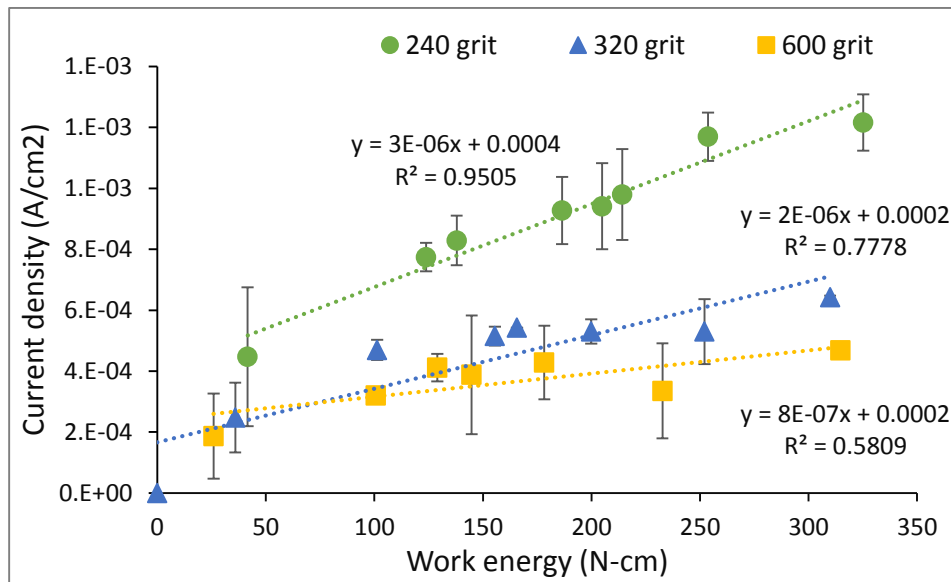


Fig 9: Average current density vs. average work done for 316LSS samples with roughness 240 grit, 320 grit and 600 grit. Note the linear relation between current density and work done, which correspond to electrochemical energy and mechanical energy respectively. Mean and SD n=3

Fig. 9 shows the linear relationship between the electrochemical work done, denoted by current density (A/cm^2) and mechanical work done, denoted by the energy dissipated in a cycle of fretting (N-cm). The linear relationship shows a proportionality between mechanical work and electrochemical currents, which is also seen in the hysteresis loops shown earlier.

3.3.4 Co-efficient of friction (COF)

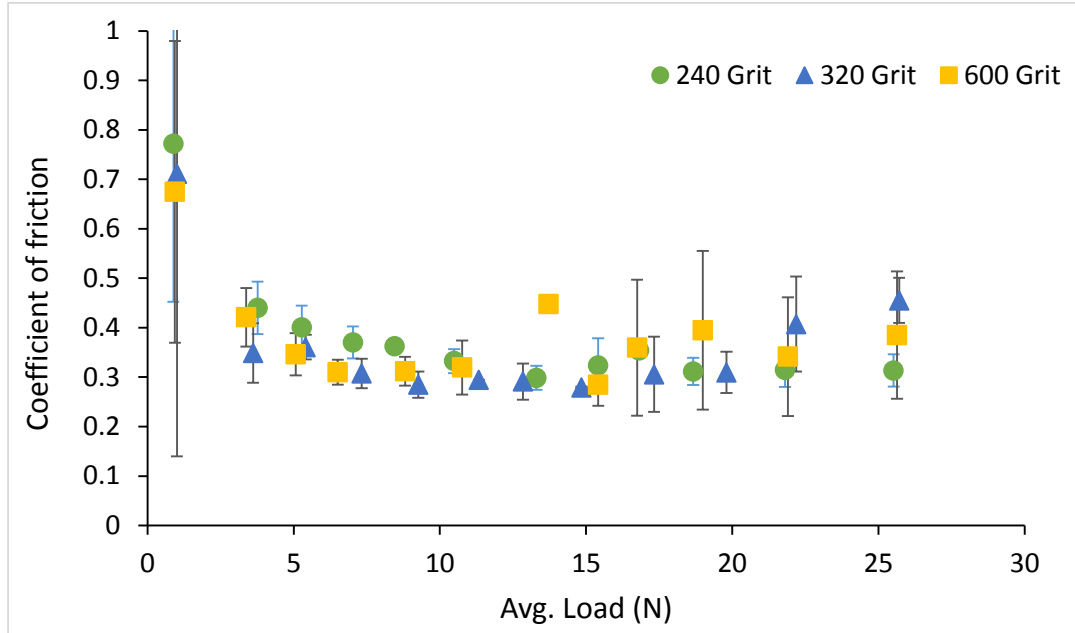


Fig 10: Average coefficient of friction vs. average load applied. To obtain this plot, the co-efficient of friction was calculated from a plot of COF vs. time. The data was divided into windows based on loads 2 N apart and averaged over this window. This average is plotted against average load. Mean and SD n=3.

The co-efficient of friction between two interfacing surfaces was between 0.3 and 0.4 and is a property of the material itself. From Fig. 10, it is evident that the COF of 316L stainless steel couples is not dependent on surface roughness, that is, the co-efficient of friction remained unchanged with change in surface roughness. Two-way ANOVA showed no statistically significant difference in the coefficients of friction based on the surface roughness. However, the coefficient of friction varied with increasing load ($p < 0.005$).

3.3.5 Fretting corrosion equation and surface roughness

As explained in chapter 2, fretting currents can be described by the factors affecting fretting behavior such as oxide characteristics and the inter-asperity distance, Δ . Changing the surface roughness is hypothesized to change the distance between consecutive asperities in contact in an interface and thus a study of how the interasperity distance changes with surface roughness and normal load is presented in the following graph:

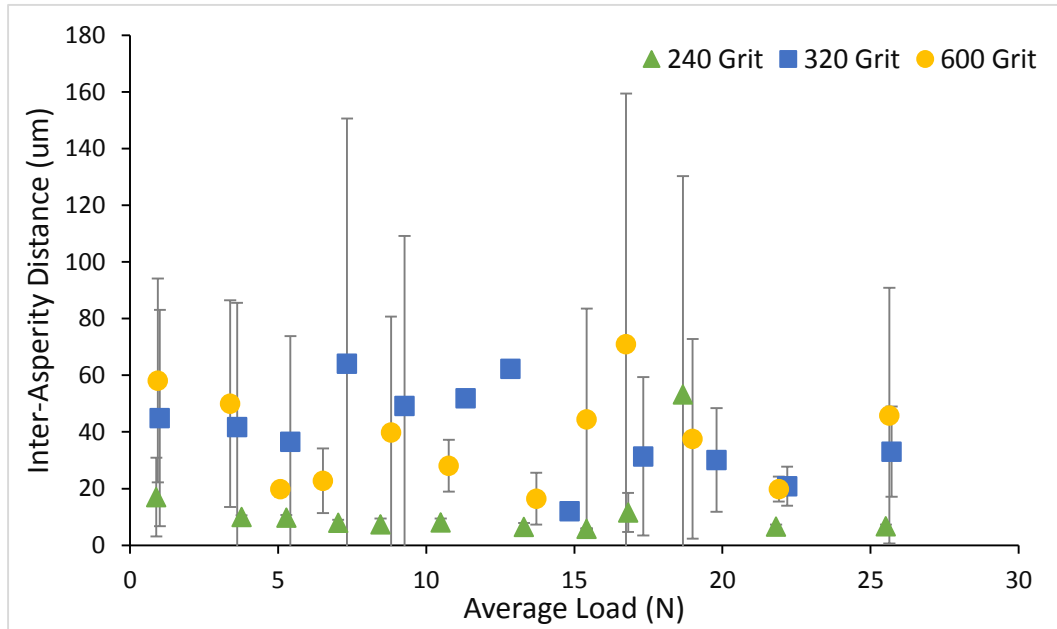


Fig 11: Average interasperity distance vs. average load. To obtain this plot, the interasperity distance for each data point was collected. The data was divided into windows based on loads 2 N apart and averaged over this window. This average is plotted against average load. Mean and SD n=3.

From Figure 11, it is seen that the inter-asperity distance decreases with the load applied, which is expected. However, there is a high degree of variation in the interasperity distance parameter as seen from the standard deviation values.

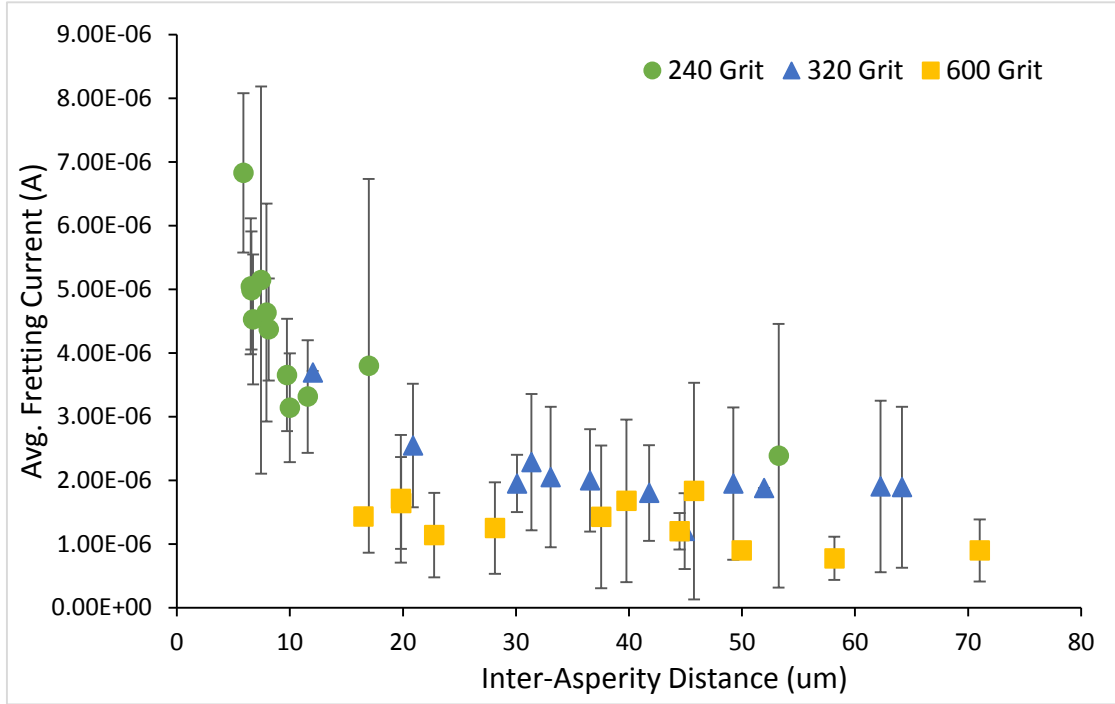


Fig. 12: Average fretting current vs. average interasperity distance. Note that the initial data points for 240 grit correspond to high fretting currents. Smoother surfaces (320 grit and 600 grit) are more distributed over a wider range of interasperity distances. Mean and SD n=3.

The fretting currents generated in the oxide film and the average interasperity distance on the surface are inversely related to each other, which can be seen in Fig. 12. The higher fretting currents seen for the rough surface (240 grit) corresponds to lower interasperity distance, Δ , and the smoother surfaces (320 grit and 600 grit) correspond to higher interasperity distance. There is a significant difference between the different surfaces in terms of Δ ($p < 0.005$). Hence, the interasperity distance parameter changes with the roughness of the surface, it is higher for rough surfaces and lower for smoother surfaces.

3.3.6 Fretted area measurement

Fretted area is the measured area on the sample surface that displays fretting scars, which is measured at the end of each fretting experiment. It gives an indication of the actual area of contact instead of the nominal area of contact.

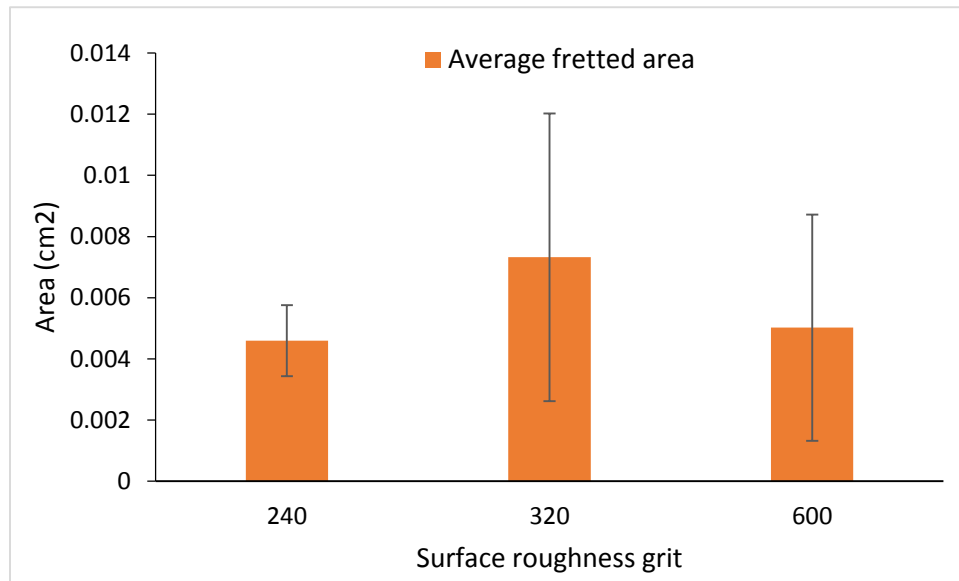


Fig. 13: Average fretted area for samples of 240 grit, 320 grit and 600 grit. Fretted area measured post fretting using SEM images and ImageJ. Mean and SD n=3

Fig 13 shows the average fretted area of all samples tested, at 240 grit, 320 grit and 600 grit. Each sample was tested with an exposed area of around 0.08717 cm^2 . The largest average fretted area corresponds to 320 grit, 0.00732 cm^2 . However, there is no significant difference between the average fretted area for different roughness ($p < 0.5$).

3.3.7 AFM measurements

The following roughness values were determined for the 240, 320 and 600 grit surfaces using contact mode AFM, as described in chapter 2.

Surface roughness grit	Ra (nm)	Rq (nm)
240	209.68 \pm 20.99	262.85 \pm 37.23
320	151.44 \pm 10.39	193.39 \pm 4.43
600	79.4 \pm 14.29	104.71 \pm 20.92

Table 4: Surface roughness parameters measured using Eqns. 2.2 and 2.3 for 316LSS coupons using AFM in contact mode. Measurements were obtained from the height images captured for an area of 25 x 25 μm . Roughness parameters corroborate the increasing smoothness of the surface with increasing grit level. Mean, SD for n=3.

The AFM allows imaging of the surface, using which the topography of the surface can be visualized. Figures 14, 15 and 16 correspond to 316L stainless steel coupons polished with 240, 320 and 600 grit paper respectively. Note the differences in the width of the scratches on the surface, which give rise to the difference in topography and roughness of the surfaces. All images denote an area on 25 x 25 μm in the central region of the coupons.

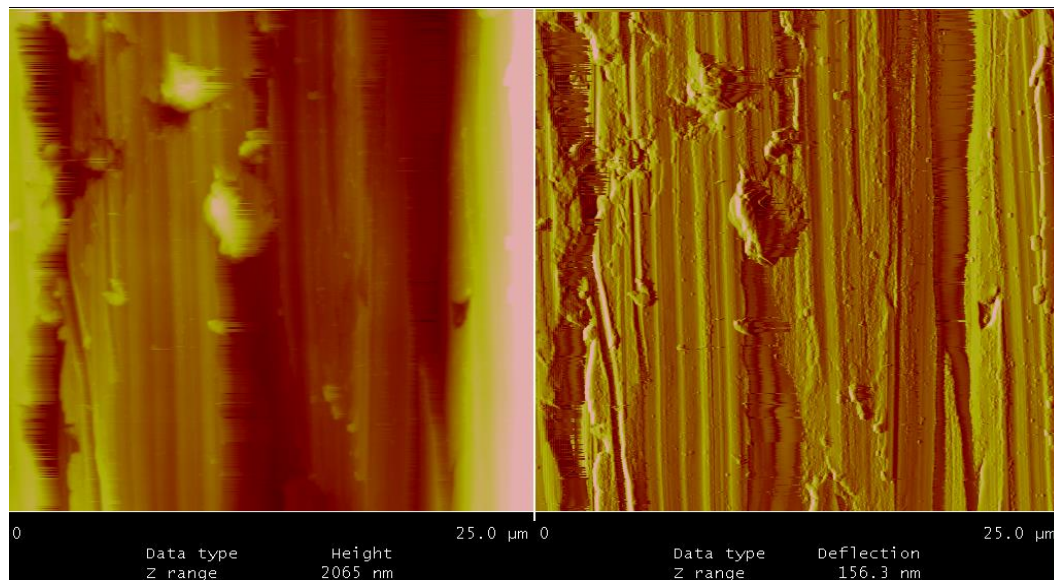


Fig 14: AFM images denoting height and deflection measurements of 316L stainless steel 240 grit surface.

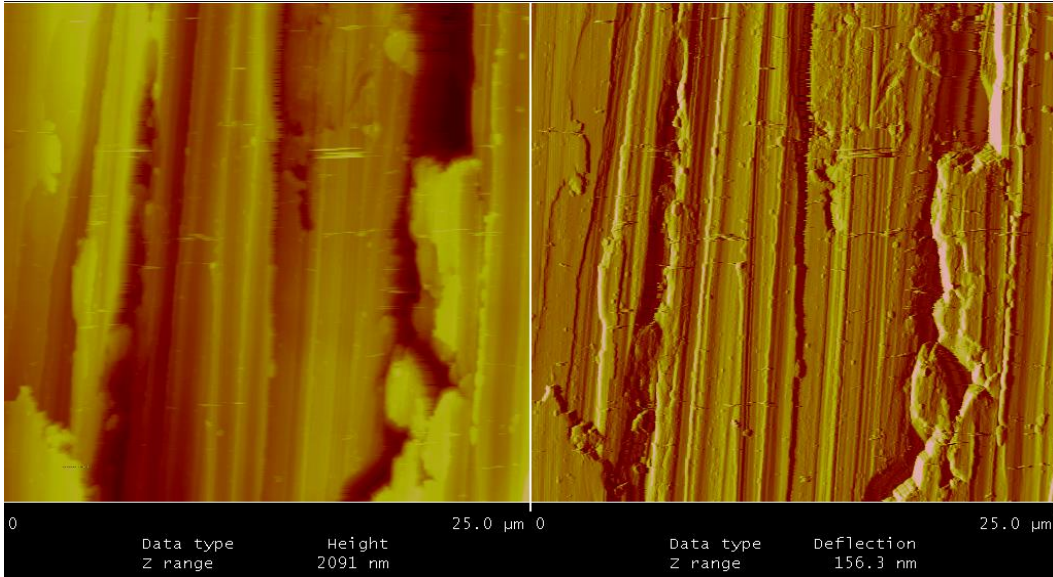


Fig 15: AFM images denoting height and deflection measurements of 316L stainless steel 320 grit surface.

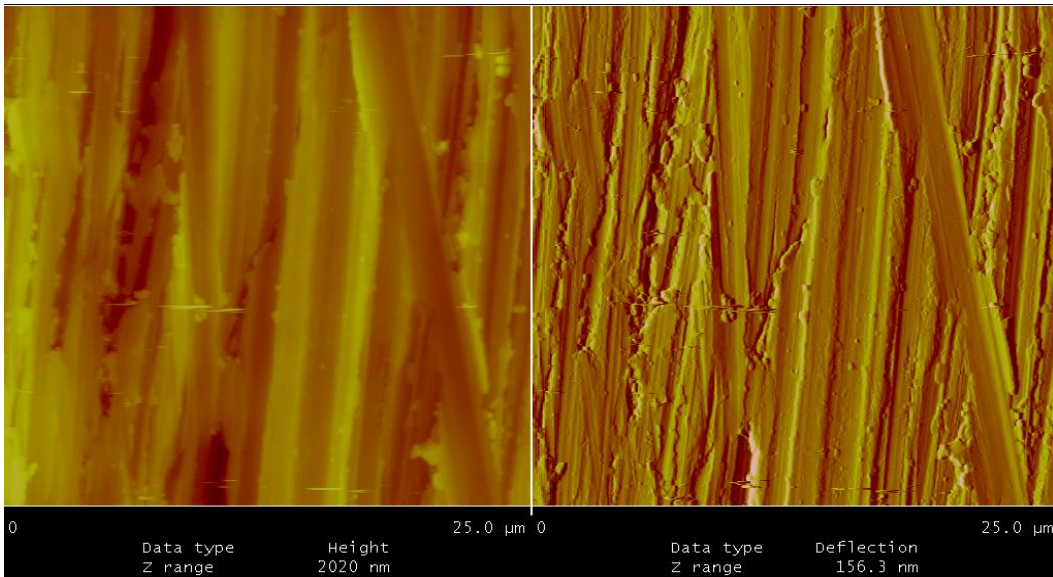


Fig 16: AFM images denoting height and deflection measurements of 316L stainless steel 600 grit surface.

3.3.8 SEM images

Visualization of the sample surfaces prior to and post testing is essential for putting the results into perspective. SEM imaging was done using both the secondary electron mode

as well as the backscatter mode to determine the true nominal area of contact and to capture the nature of the damage.

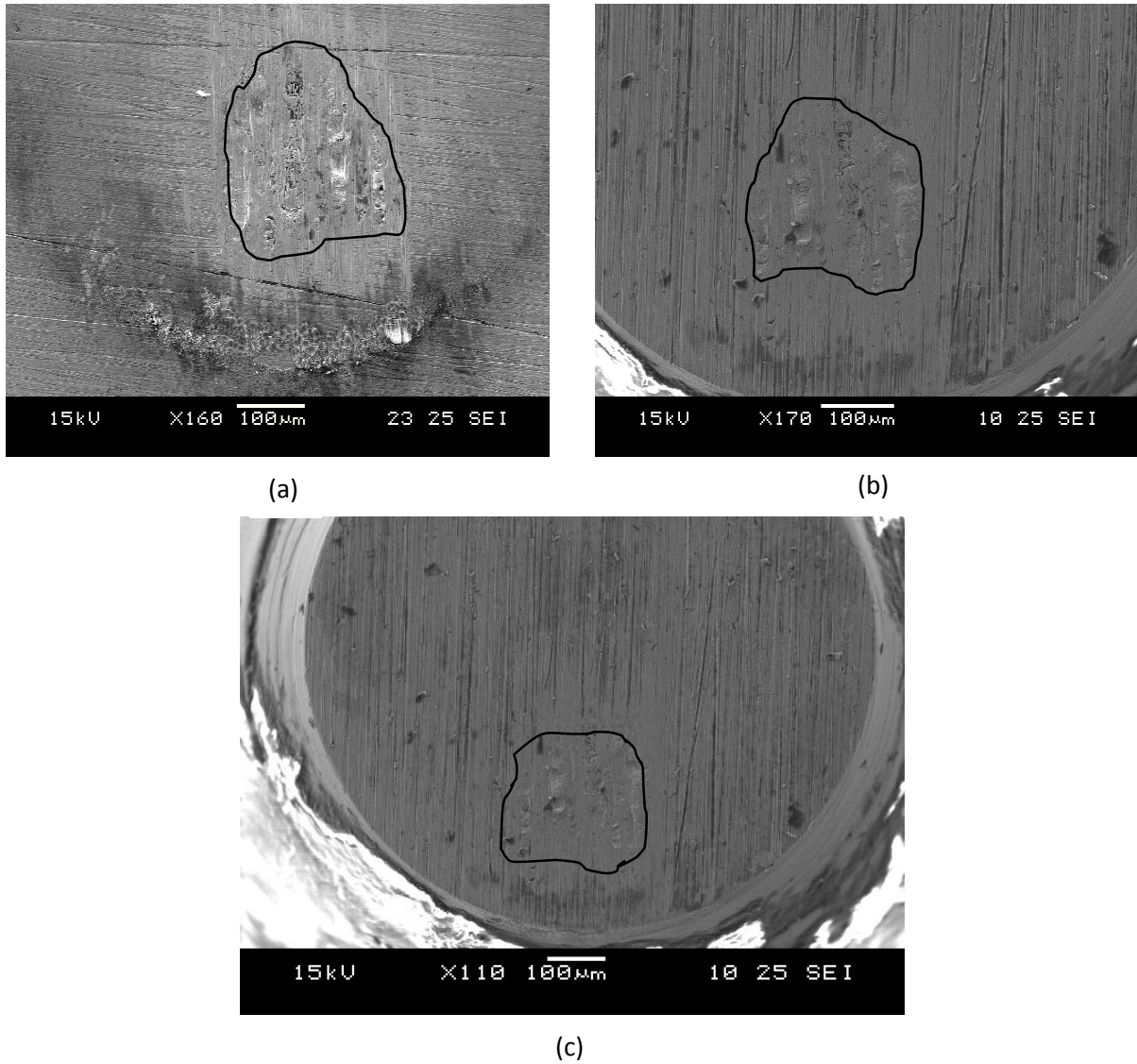


Fig 17: Secondary electron SEM micrographs of (a) pin and (b) disc with 600 grit surface roughness post test (c) low magnification image of pin showing actual area of contact (marked). Note the actual area of contact displaying fretting scars and the deposition adjacent to fretted area.

Figures 17 (a) and 17 (b) show the superimposable fretted area on a pin-disc couple. Note the perpendicularity of the grit lines on the pin and disc surface. The regions in contact on both are mirror images demonstrating that only the area in contact with the interfacing

surface undergoes scarring. In Fig. 17 (c) the actual fretted area is visible as opposed to the entire area of the pin which is interfacing with the disc. Thus, the area in contact can be thought of as discrete asperities in contact rather than an entire surface. Imaging revealed the presence of oxides and salts on and near the fretted area, which are by-products of the reduction and oxidation reactions at the surface, as well as fretting scars.

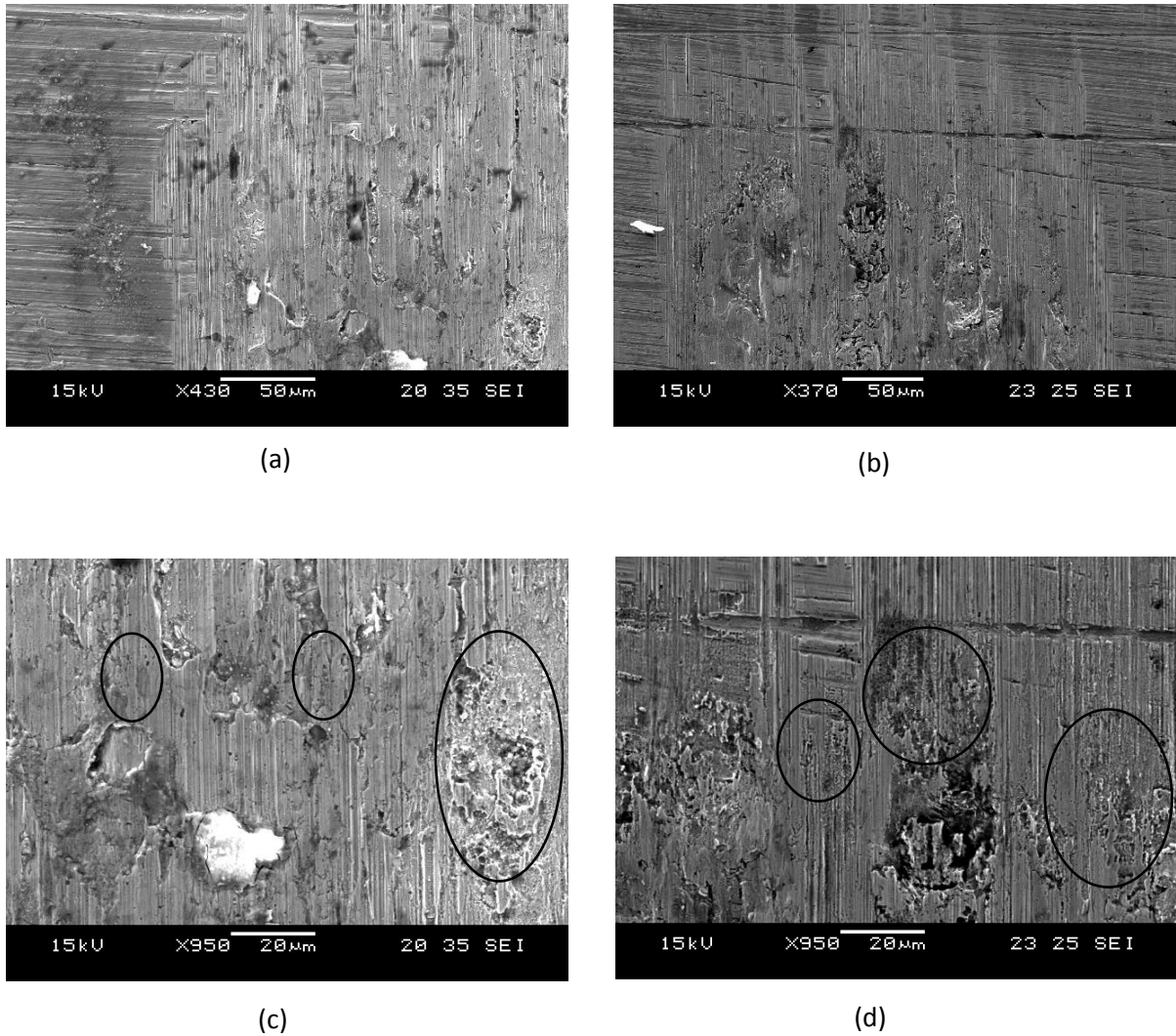


Fig 18: Secondary electron SEM micrographs of (a) 240 grit disc (b) 600 grit disc (c) magnified region of disc in (a) and (d) magnified image of disc in (b). Note the pitting in (c) and (d) (circled in black).

Fig. 18 consists of representative images showing evidence of pitting observed in all of the samples tested reflecting the ongoing crevice corrosion after fretting stopped.

Although pitting was observed in every sample tested, it occurred to a greater degree in the smoother surface (600 grit) than in the rougher surface which is consistent with the recovery current measurements described earlier. Evidence of plastic deformation is also visible in the SEM micrographs, and there seems to be more surface damage on the smoother surface than on the rough surface.

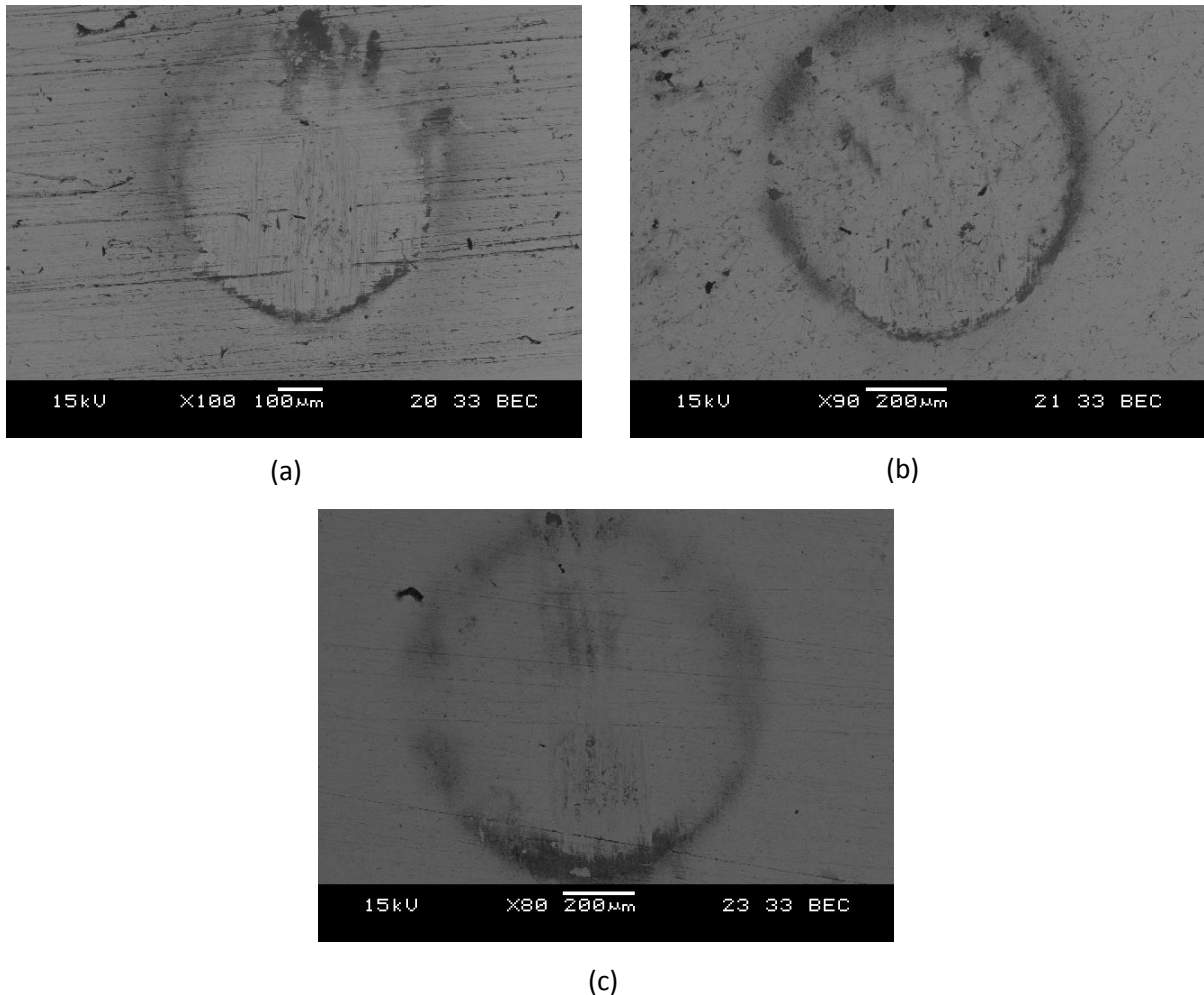


Fig 19: Backscattered electron SEM micrographs of (a) 240 grit disc (b) 320 grit disc (c) 600 grit disc post-test. Note the ‘halo’ of the pin on disc surface.

Figure 19 (a), 16 (b) and 16 (c) show backscattered images of sample discs of 240 grit, 320 grit and 600 grit respectively. The ‘halo’ seen in these images are due to the oxidation and reduction reactions that occur during corrosion, causing deposition of ions and salts as well as loss of metal into the surrounding fluid.

3.4 Discussion

Fretting corrosion and its mechanisms have been explored in several studies from different perspectives [11], [32], [37]–[39]. There is still a need to understand how the surface roughness affects the fretting corrosion behavior of devices and vice versa. This study was undertaken in order to investigate the effects of surface roughness on the fretting crevice corrosion response of 316LSS. This study also looked at the role of nominal contact stress on the fretting corrosion and fretting initiated crevice corrosion. The effects of changing normal load between surfaces has been studied previously [19], [22] and is corroborated with this study. The results show how the currents generated with increasing load showed an initial rise, followed by a gradual decrease. Viswanathan and Gilbert in 2012 conducted a study to study the effects of applied normal load on fretting corrosion behavior and found similar behavior in CoCrMo/Ti6Al4V, Ti6Al4V/Ti6Al4V and CoCrMo/CoCrMo combinations. The study attributed this behavior to the changes in contact stresses developed as a result of the load, where initially the contact stresses do not enough oxide fracture to generate high enough currents but increasing loads induce higher stresses causing more damage, and hence, higher currents. At higher loads, however, sticking of the pin and disc hinder the sliding and the abrasion of the oxide layer, leading to a gradual decline in the currents.

In this study, surfaces of the stainless steel couples tested were polished to different roughness values and subjected to a pin-on-disk fretting corrosion test where the normal load was increased in steps and a 50 μm cyclic micromotion was induced. Fretting currents were measured during and in between subsequent fretting cycles. It was seen that the average fretting current changed significantly with the surface roughness ($p < 0.05$) with

lower currents seen at lower roughness. However, the crevice corrosion induced by fretting corrosion after the fretting motion was stopped, was more prolonged and had a lower onset load at lower roughness. This study found that the interfacial friction seems to be unaffected by the roughness. Rougher surfaces, or surfaces with a higher value of roughness parameter R_a , offers more frictional resistance than a smooth surface, for example, the resistance offered by sandpaper is higher than that by glass. This does not seem to be the case during fretting corrosion. In this test, this behavior may be because of the perpendicular orientation of the grit lines on opposing surfaces or because the fretting caused damage to the surface and diminished the overall effects of roughness.

Another possible explanation for this phenomenon is the difference between the actual area in contact and the nominal area in contact at the interface. It is hypothesized that the area in contact can be considered as a set of individual asperities in contact and undergoing fretting. Thus, there is a correlation between the average distance between these asperities, called the interasperity distance and denoted by Δ , and the fretting currents that arise as a result of the corrosion [22], they are inversely related and this is seen in Fig. 11. The values of Δ for surfaces of different roughness is not statistically significant, as seen in the results. The calculated Δ is a function of the measured nominal area post fretting, which was measured using SEM images and the ImageJ software in this study. It is worthwhile to note that the fretted area measured in this way, does not take into account the peaks and troughs that are bound to be present on the surface. How the fretting motion and corrosion reactions contribute to the wear and the destruction of the scratches on the surface that contribute to the roughness and the actual area of contact is a subject for further study.

From the images obtained using the AFM, the surface topographies can be seen prior to fretting. There is a marked difference in the distances between subsequent scratches on the surfaces of different roughness, which explains the difference in the way the surfaces interact to give rise to fretting corrosion behavior. At the same time, investigation of the changes wrought by the fretting corrosion has not been conducted as part of this study. Interactions between interfacing surfaces can be expected to cause wearing down of the peaks seen from the images, which would modify the topography and change the surface area in contact. Acquiring images from different samples, all prepared in an identical manner, will be more descriptive of the surface topography; however, since the polishing is manual, there can be noticeable difference among different samples obtained thus. Several factors such as applied pressure, direction of polishing as well as the characteristics of the grit paper used will have a bearing upon the final surface obtained.

Further investigation of how different topographies can be used to mitigate fretting corrosion behavior is required. A possible direction could be to explore the creation of smooth undulations on the surface of the device. This would enforce smoother surfaces, with asperities set a larger distance apart thus reducing the average fretting current. However, it is important to note the consequences of the modification of the surface topography on the interfacial friction and the formation of crevice conditions within the topography. Surface roughness which is a quantification of the topography is an excellent tool to study the effects of changing the topography at a micro or even nano-scale. Consideration must also be given to the alignment of the grit lines on the surfaces. This study was conducted using perpendicular alignment of grit lines on the pin and disk surface. Transverse or parallel alignment would impact the interaction of the surfaces as well as the

effective roughness of the surfaces. Formation of crevices within the interface and their geometry and shape is dependent on the surface topography. Further investigation should be made in this direction as well.

While considering modifications for the surface the interfacial friction is another vital factor that has direct bearing on the fretting behavior as well as oxide abrasion. Completely eliminating the friction is one way of eliminating the possibility of oxide abrasion. However this is not practically achievable, even with tight fitting modular parts. It might be worthwhile to explore the possibility of creating surfaces that are unable to slide easily against each other, thus creating a sticky interface. In order to account for the bending of the device due to applied loads and to maintain compliance matching with the native tissue, the material needs to be compliant enough to convey the natural motion joints undergo during routine activities. Hence sticky-compliance might be a viable alternative to eliminating friction by creating tight fitted modular parts.

There are efforts being made elsewhere to study the surface of orthopedic devices and to investigate the improvement in corrosion resistance of these devices by use of coatings and surface treatments that modify the roughness of the surface [40]–[42]. These studies focus on the changes in roughness brought on by corrosion reactions at the surface or by surface treatments and coatings. The unique feature of this study is the investigation of the effects of changing roughness on fretting corrosion behavior of 316LSS alloy. This study provides insight into the possible mechanisms by which roughness influences corrosion. The next step would be to investigate how the corrosion reactions modify the area in contact to either change its morphology and topography or to modify the effect it has on further fretting corrosion behavior of the surface.

3.5 Conclusion

The primary conclusions that can be made from this study are:

- a. Interfacial co-efficient of friction is not a function of the surface roughness.
- b. Fretting corrosion behavior is dependent on the surface roughness and the topography of the surfaces interfacing with each other.
- c. Fretting currents are dependent on the surface roughness and topography. Higher fretting currents are generated for rougher surfaces and vice versa.
- d. Fretting-initiated crevice corrosion was observed in all couples, irrespective of surface roughness. However lower onset loads and more prolonged crevice corrosion was observed for smoother surfaces.

The fretted area is an important factor throughout a fretting corrosion experiment. Fretting at the surface brings about degradation of the scratches induced in the surface during surface preparation, and this in turn continuously changes the area available for contact throughout the experiment.

4. SUMMARY

Fretting corrosion, a form of mechanically-assisted corrosion, is a problem faced by the medical device industry. It is a form of corrosion brought about by micromotion of two surfaces in close contact, which leads to abrasion of the oxide film on the surface of orthopedic alloys. The consequences of fretting corrosion include, but are not limited to, fracture of the passivating oxide film, corrosion of underlying substrate, wear and debris generation, all of which ultimately lead to the failure of the device, necessitating revision surgery.

Studies have been conducted to determine the factors that cause and aggravate fretting corrosion conditions in vivo. Some of these factors are the applied load at the interface, potential of the surfaces in contact and solution chemistry. This study focuses on surface roughness as a factor affecting fretting corrosion behavior of 316L stainless steel alloy. Variable load pin-on-disc fretting tests are conducted under potentiostatic conditions and physiological pH to determine the fretting currents generated at the surfaces of a pin and disc, and how these currents vary with roughness. The pins and discs were sanded to create surfaces with roughness of 240 grit, 320 grit and 600 grit, 240 grit being the roughest.

It was found that fretting currents are highest for 240 grit and lowest for 600 grit. The dependence of fretting currents on roughness is statistically significant ($p < 0.005$). The work done during fretting varies with the nominal contact stress, demonstrating the fretting regimes of full slip, partial slip and full stick. Fretting initiated crevice corrosion is also observed in all samples, with 600 grit samples showing lowest onset loads (around 1 N). The crevice corrosion was more prolonged and recovery currents were higher relative to fretting

currents for 600 grit. Coefficient of friction is not a function of surface roughness and neither is the interasperity distance. There is, however, an inverse relation between interasperity distance and fretting currents.

This study provided significant insight into the correlation between surface roughness and fretting corrosion behavior. Further study of the effects of corrosion reactions on the change in roughness during a fretting corrosion test is forthcoming. Another topic for further study is the influence of surface topography on fretting corrosion parameters, like fretting currents, interasperity distance, contact stresses and so on.

5. APPENDIX

The following figure is a screenshot of the NI LabVIEW program used in the data collection.

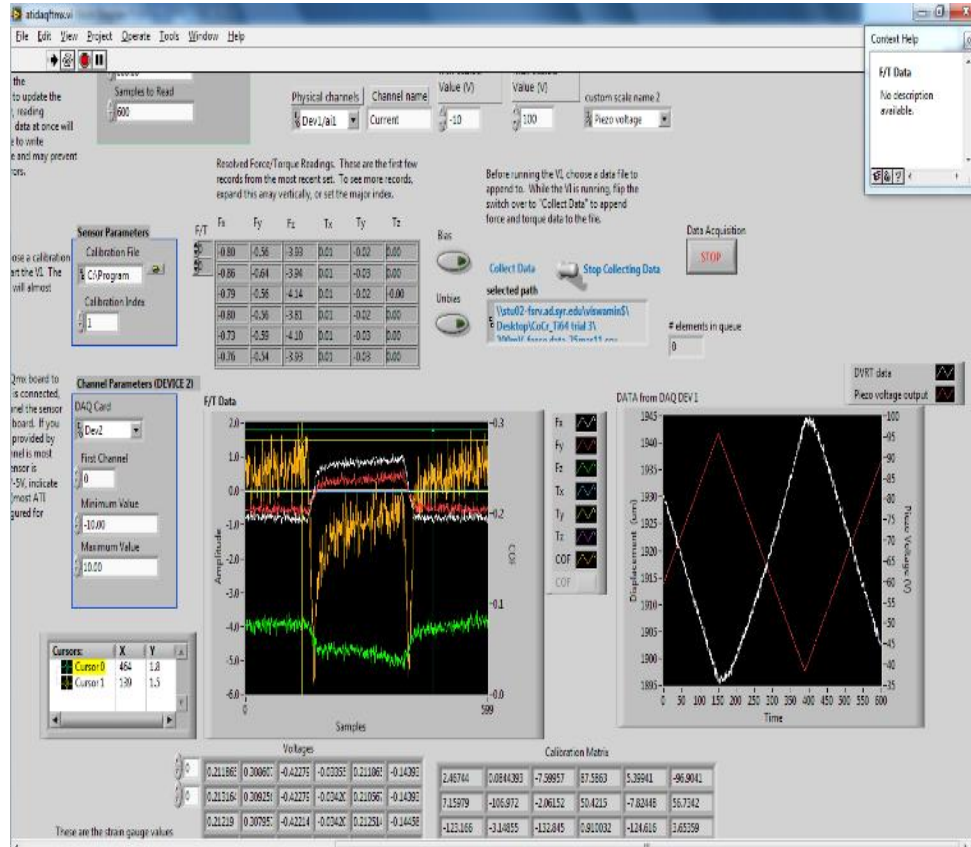


Fig 20: NI LabVIEW program window for mechanical data collection. The plots in the left window show normal load (green), co-efficient of friction (yellow). The plots in the right window show piezoelectric input to the stage (red) and DVRT measurement (white).

The following figure is a screenshot of the CorrWare window, showing the experimental setup and the electrochemical cell setup.

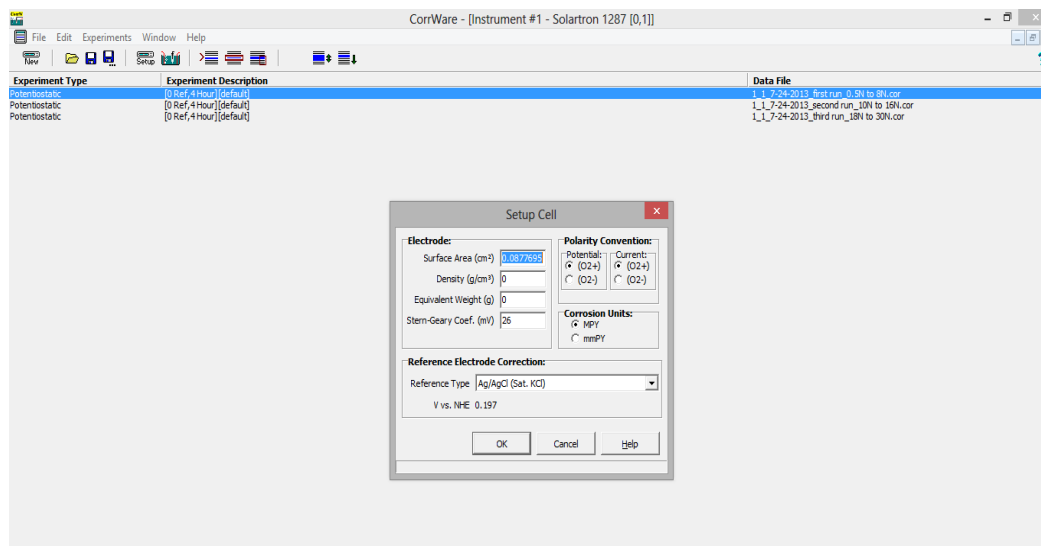


Fig 21: Screenshot of experimental setup in CorrWare. Experiment is divided into three sections, based on applied normal load: (a) 0.5N-8N (b) 10N-16N (c) 18N-30N.

During each section, current is measured during fretting for each load level. Prior to the experiment, the electrochemical cell is set up with the exposed surface area, reference electrode used and so on.

The test system described earlier was designed and developed in-house, as shown in Fig. 19. It is a custom built equipment for performing pin-on-disc fretting corrosion tests, and has the capability to house samples of varying diameters (20 mm to 35 mm discs). The linear X-Y stage and the electrochemical chamber is mounted on a thick aluminum base for additional support.

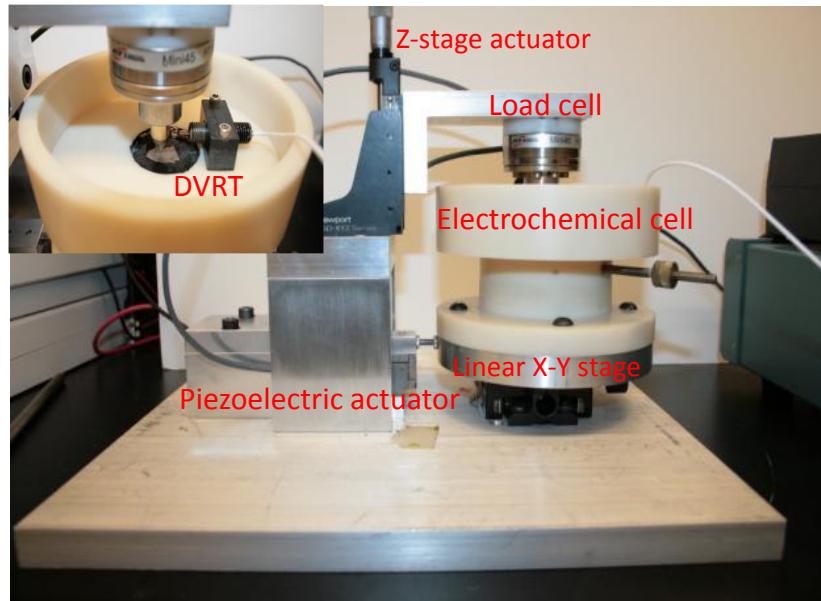


Fig 22: Image of pin-on-disc fretting test system. Some of the primary components are labelled in red. Inset shows the inside of the electrochemical cell with the sample pin and disc as well as the DVRT.

Figures 23 (a)-(i) show the individual fretting loops displaying tangential force vs. displacement for all samples tested. Each figure shows loops corresponding to five loads for which data was recorded.

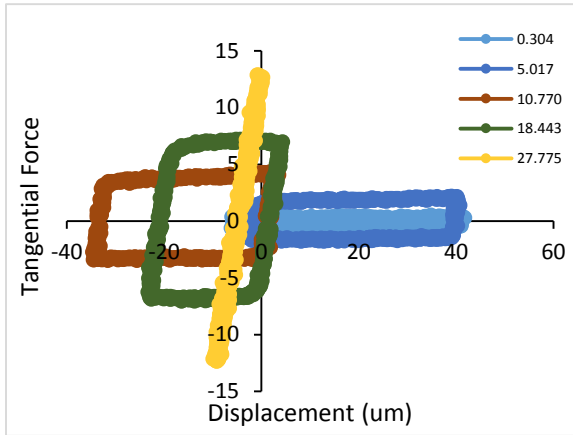


Fig 23 (a): Fretting loops 240 grit Test 1

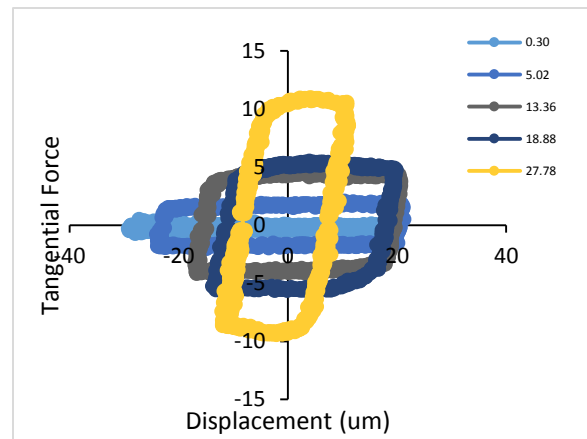


Fig 23 (b): Fretting loops 240 grit Test 2

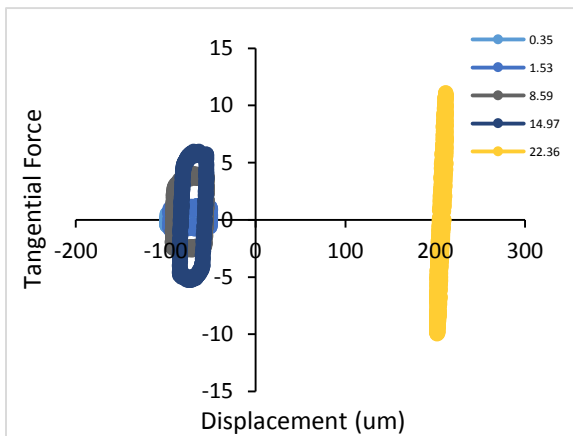


Fig 23 (c): Fretting loops 240 grit Test 3

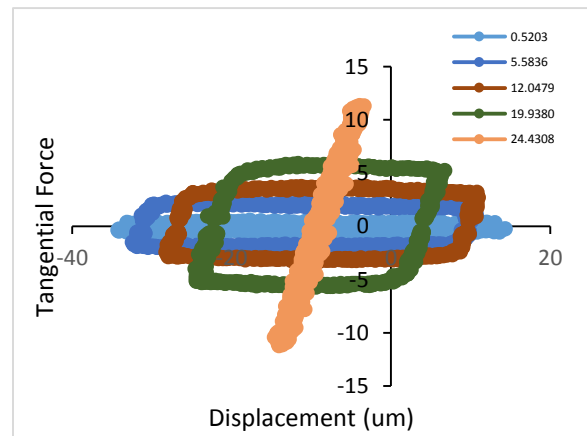


Fig 23 (d): Fretting loops 320 grit Test 1

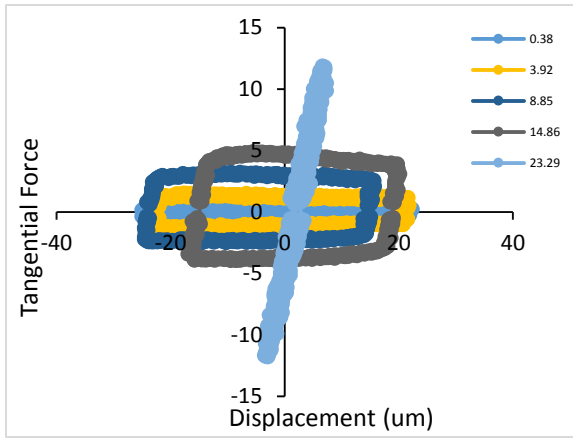


Fig 23 (e): Fretting loops 320 grit Test 2

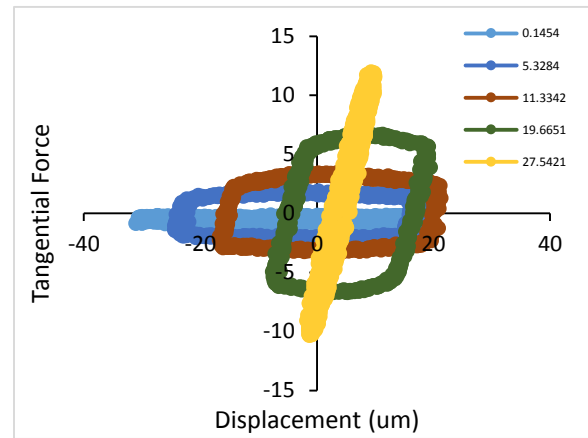


Fig 23 (f): Fretting loops 320 grit Test 3

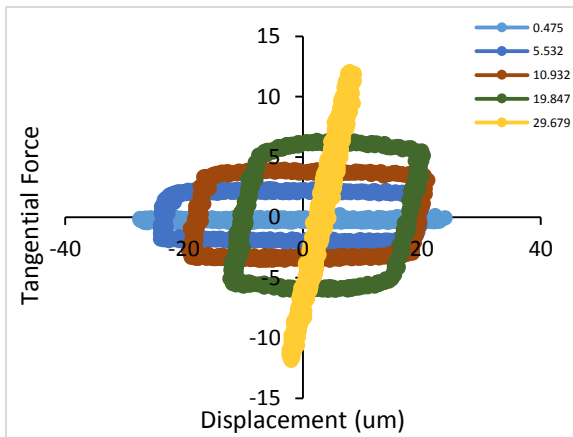


Fig 23 (g): Fretting loops 600 grit Test 1

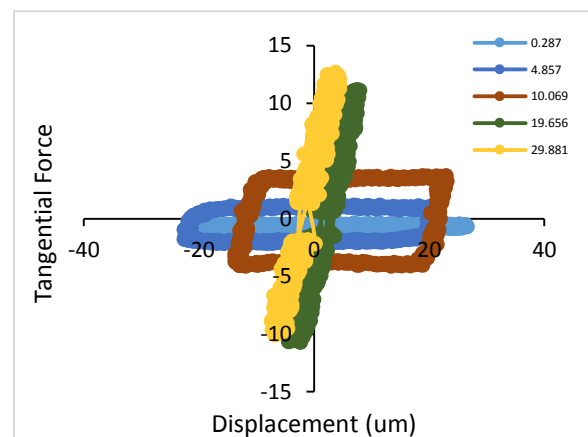


Fig 23 (h): Fretting loops 600 grit Test 2

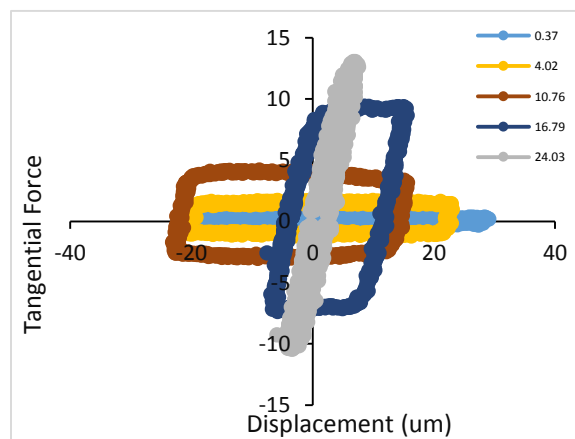


Fig 23 (i): Fretting loops 600 grit Test 3

Figures 24 (a)-(c) show the fretting current results for individual trials plotted against applied normal load. The high standard deviations are explained by the cyclic nature of the current as well as the noise generated in the system during the test.

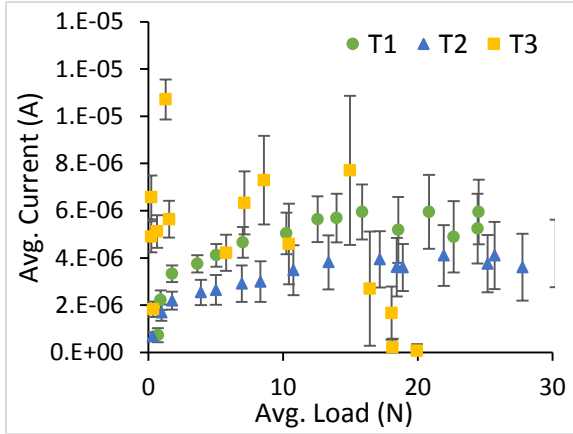


Fig 24 (a): Avg. current vs. avg. load for 240 grit samples (n=3)

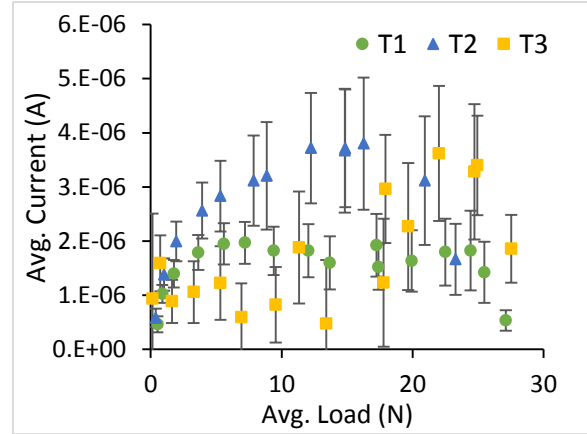


Fig 24 (b): Avg. current vs. avg. load for 320 grit samples (n=3)

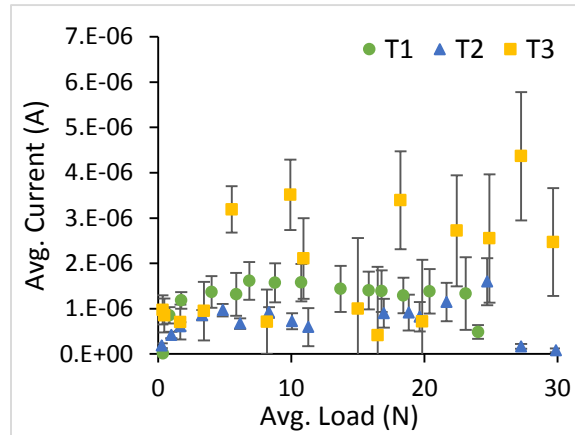


Fig 24 (c): Avg. current vs. avg. load for 600 grit samples (n=3)

6. BIBLIOGRAPHY

- [1] J. R. Goldberg, J. L. Gilbert, J. J. Jacobs, T. W. Bauer, W. Paprosky, and S. Leurgans, “A multicenter retrieval study of the taper interfaces of modular hip prostheses.,” *Clin. Orthop. Relat. Res.*, no. 401, pp. 149–161, 2002.
- [2] S. Munir, M. B. Cross, C. Esposito, A. Sokolova, and W. L. Walter, “Corrosion in modular total hip replacements: An analysis of the head-neck and stem-sleeve taper connections,” vol. 24, no. 4. pp. 240–245, 2013.
- [3] C. D. Griffin, R. A. Buchanan, and J. E. Lemons, “In vitro electrochemical corrosion study of coupled surgical implant materials.,” *J. Biomed. Mater. Res.*, vol. 17, no. 3, pp. 489–500, 1983.
- [4] R. S. Boggan, J. E. Lemons, and E. D. Rigney, “Clinical and laboratory investigations of fretting and corrosion of a three-component modular femoral stem design.,” *J. Long-term Eff. Med. Implant.*, vol. 4, no. 4, pp. 177–191, 1994.
- [5] R. Venugopalan, T. A. Justice, L. C. Lucas, and J. E. Lemons, “Galvanic corrosion in modular THRs: correlating in-vitro test results to observations from retrieval analyses,” 1997, pp. 481–484.
- [6] U. Vieweg, D. van Roost, H. K. Wolf, C. A. Schyma, and J. Schramm, “Corrosion on an internal spinal fixator system.,” *Spine*, vol. 24, no. 10, pp. 946–951, 1999.
- [7] D. C. Rodrigues, R. M. Urban, J. J. Jacobs, and J. L. Gilbert, “In vivo severe corrosion and hydrogen embrittlement of retrieved modular body titanium alloy hip-implants,” vol. 88, no. 1. pp. 206–219, 2009.
- [8] T. P. Hoar and D. C. Mears, “Corrosion-Resistant Alloys in Chloride Solutions: Materials for Surgical Implants,” *Proceedings of the Royal Society of London. Series A.*

Mathematical and Physical Sciences, vol. 294, no. 1439. pp. 486–510, 1966.

[9] L. Savarino, G. S. Maci, M. Greco, N. Baldini, and A. Giunti, “Metal ion release from fracture fixation devices: a potential marker of implant failure.,” *J. Biomed. Mater. Res. Part B, Appl. Biomater.*, vol. 86, no. 2, pp. 389–395, 2008.

[10] D. M. Jones, J. L. Marsh, J. V. Nepola, J. J. Jacobs, A. K. Skipor, R. M. Urban, J. L. Gilbert, and J. A. Buckwalter, “Focal osteolysis at the junctions of a modular stainless-steel femoral intramedullary nail.,” *J. bone Jt. surgery. Am. Vol.*, vol. 83-A, no. 4, pp. 537–548, 2001.

[11] N. Diomidis and S. Mischler, “Third body effects on friction and wear during fretting of steel contacts,” *Tribol. Int.*, vol. 44, pp. 1452–1460, 2011.

[12] J. L. Gilbert and J. J. Jacobs, “The mechanical and electrochemical processes associated with taper fretting crevice corrosion: A review,” vol. 1301. pp. 45–59, 1997.

[13] C. G. Mohler, J. J. Callaghan, D. K. Collis, and R. C. Johnston, “Early loosening of the femoral component at the cement-prosthesis interface after total hip replacement.,” *J. bone Jt. surgery. Am. Vol.*, vol. 77, no. 9, pp. 1315–1322, 1995.

[14] S. A. Brown, C. A. Flemming, J. S. Kawalec, H. E. Placko, C. Vassaux, K. Merritt, J. H. Payer, and M. J. Kraay, “Fretting corrosion accelerates crevice corrosion of modular hip tapers.,” *J. Appl. Biomater. : Off. J. Soc. Biomater.*, vol. 6, no. 1, pp. 19–26, 1995.

[15] J. Walczak, F. Shahgaldi, and F. Heatley, “In vivo corrosion of 316L stainless-steel hip implants: morphology and elemental compositions of corrosion products.,” *Biomaterials*, vol. 19, no. 1–3, pp. 229–237, 1998.

[16] S. A. Brown and J. P. Simpson, “Crevice and fretting corrosion of stainless-steel plates and screws.,” *J. Biomed. Mater. Res.*, vol. 15, no. 6, pp. 867–878, 1981.

- [17] E. B. Mathiesen, J. U. Lindgren, G. G. Blomgren, and F. P. Reinholt, "Corrosion of modular hip prostheses.," *J. bone Jt. surgery. Br. Vol.*, vol. 73, no. 4, pp. 569–575, 1991.
- [18] V. Guiñón-Pina, A. Igual-Muñoz, and J. García-Antón, "Influence of pH on the electrochemical behaviour of a duplex stainless steel in highly concentrated LiBr solutions," vol. 53, no. 2. pp. 575–581, 2011.
- [19] S. C. Jani, W. L. Sauer, T. W. McLean, R. D. Lambert, and P. Kovacs, "Fretting corrosion mechanisms at modular implant interfaces," vol. 1301. pp. 211–225, 1997.
- [20] J. L. Gilbert, S. Mali, R. M. Urban, C. D. Silvertown, and J. J. Jacobs, "In vivo oxide-induced stress corrosion cracking of Ti-6Al-4V in a neck-stem modular taper: Emergent behavior in a new mechanism of in vivo corrosion," *J. Biomed. Mater. Res. Part B: Appl. Biomater.*, vol. 100B, pp. 584–594, 2012.
- [21] J. L. Gilbert, C. A. Buckley, and J. J. Jacobs, "In vivo corrosion of modular hip prosthesis components in mixed and similar metal combinations. The effect of crevice, stress, motion, and alloy coupling.," *J. Biomed. Mater. Res.*, vol. 27, no. 12, pp. 1533–1544, 1993.
- [22] V. Swaminathan and J. L. Gilbert, "Fretting corrosion of CoCrMo and Ti6Al4V interfaces.," *Biomaterials*, vol. 33, no. 22, pp. 5487–5503, 2012.
- [23] M. T. Ehrensberger and J. L. Gilbert, "The effect of static applied potential on the 24-hour impedance behavior of commercially pure titanium in simulated biological conditions," vol. 93, no. 1. pp. 106–112, 2010.
- [24] E. Brooks, M. Tobias, K. Krautsak, and M. Ehrensberger, "The influence of cathodic polarization and simulated inflammation on titanium electrochemistry." 2014.
- [25] B. Hashemi, M. Rezaee Yazdi, and V. Azar, "The wear and corrosion resistance of shot peened-nitrided 316L austenitic stainless steel," vol. 32, no. 6. pp. 3287–3292, 2011.

- [26] S.-H. Chang, J.-Z. Chen, S.-H. Hsiao, and G.-W. Lin, "Nanohardness, corrosion and protein adsorption properties of CuAlO₂ films deposited on 316L stainless steel for biomedical applications," vol. 289. pp. 455–461, 2014.
- [27] K. Alrbaey, D. Wimpenny, R. Tosi, W. Manning, and A. Moroz, "On Optimization of Surface Roughness of Selective Laser Melted Stainless Steel Parts: A Statistical Study." 2014.
- [28] C. Camurri, A. Gallegos, and C. Carrasco, "Rolling of 316L Stainless Steel with Rough Rolls to Potentially Obtain Superficial Nanograins." 2014.
- [29] E. Karamian, A. Khandan, M. R. Kalantar Motamedi, and H. Mirmohammadi, "Surface Characteristics and Bioactivity of a Novel Natural HA/Zircon Nanocomposite Coated on Dental Implants.," *BioMed Res. Int.*, vol. 2014, Apr. 2014.
- [30] V. S. Dhandapani, E. Thangavel, M. Arumugam, K. S. Shin, V. Veeraraghavan, S. Y. Yau, C. Kim, and D.-E. Kim, "Effect of Ag content on the microstructure, tribological and corrosion properties of amorphous carbon coatings on 316L SS," vol. 240. pp. 128–136, 2014.
- [31] M. Conradi, A. Kocijan, D. Kek-Merl, M. Zorko, and I. Verpoest, "Mechanical and anticorrosion properties of nanosilica-filled epoxy-resin composite coatings," vol. 292. pp. 432–437, 2014.
- [32] R. A. Gittens, T. McLachlan, R. Olivares-Navarrete, Y. Cai, S. Berner, R. Tannenbaum, Z. Schwartz, K. H. Sandhage, and B. D. Boyan, "The effects of combined micron-/submicron-scale surface roughness and nanoscale features on cell proliferation and differentiation.," *Biomaterials*, vol. 32, no. 13, pp. 3395–3403, 2011.
- [33] G. Zhao, A. L. Raines, M. Wieland, Z. Schwartz, and B. D. Boyan, "Requirement for

- both micron- and submicron scale structure for synergistic responses of osteoblasts to substrate surface energy and topography.,” *Biomaterials*, vol. 28, no. 18, pp. 2821–2829, 2007.
- [34] M. Göttlicher, M. Rohnke, A. Helth, T. Leichtweiß, T. Gemming, A. Gebert, J. Eckert, and J. Janek, “Controlled surface modification of Ti-40Nb implant alloy by electrochemically assisted inductively coupled RF plasma oxidation.,” *Acta Biomater.*, vol. 9, no. 11, pp. 9201–9210, 2013.
- [35] J. Chen, J. Wang, and H. Yuan, “Morphology and performances of the anodic oxide films on Ti6Al4V alloy formed in alkaline-silicate electrolyte with aminopropyl silane addition under low potential,” vol. 284. pp. 900–906, 2013.
- [36] O. Vingsbo and S. Söderberg, “On fretting maps,” vol. 126, no. 2. pp. 131–147, 1988.
- [37] S. Mischler, “Triboelectrochemical techniques and interpretation methods in tribocorrosion: A comparative evaluation,” vol. 41, no. 7. pp. 573–583, 2008.
- [38] M. T. Ehrensberger and J. L. Gilbert, “The effect of static applied potential on the 24-hour impedance behavior of commercially pure titanium in simulated biological conditions,” *J. Biomed. Mater. Res. Part B: Appl. Biomater.*, vol. 9999B, 2010.
- [39] E. Blasco-Tamarit, A. Igual-Muñoz, J. G. Antón, and D. García-García, “Effect of temperature on the corrosion resistance and pitting behaviour of Alloy 31 in LiBr solutions,” vol. 50, no. 7. pp. 1848–1857, 2008.
- [40] N. D. Nam, M. Vaka, and N. Tran Hung, “Corrosion behavior of TiN, TiAlN, TiAlSiN-coated 316L stainless steel in simulated proton exchange membrane fuel cell environment,” vol. 268. pp. 240–245, 2014.
- [41] C. Vasilescu, P. Drob, E. Vasilescu, I. Demetrescu, D. Ionita, M. Prodana, and S. I.

Drob, “Characterisation and corrosion resistance of the electrodeposited hydroxyapatite and bovine serum albumin/hydroxyapatite films on Ti-6Al-4V-1Zr alloy surface,” *Corrosion Science*, vol. 53, no. 3. pp. 992–999, Mar-2011.

[42] R. Walter, M. B. Kannan, Y. He, and A. Sandham, “Effect of surface roughness on the in vitro degradation behaviour of a biodegradable magnesium-based alloy,” *Applied Surface Science*, vol. 279, no. 0. pp. 343–348, 15-Aug-2013.

7. VITA

NAME OF AUTHOR: Aarti Shenoy
PLACE OF BIRTH: Mumbai, INDIA
DATE OF BIRTH: June 17, 1990
CONTACT INFORMATION: aashenoy@syr.edu

EDUCATION:

2012-Current Syracuse University Syracuse, NY

Enrolled in M.S. and Ph.D. program in Bioengineering, Current GPA: 3.55

- Advisor: Jeremy Gilbert, PhD

2008-2012 University of Mumbai Mumbai, India

B.E. in Biomedical Engineering

- Graduated with Distinction

PROFESSIONAL MEMBERSHIPS:

- Student member, Society for Biomaterials